

1 **Rab5 and Alsin regulate stress-activated cytoprotective signaling on mitochondria**

2

3 FoSheng Hsu¹, Stephanie Spann¹, Charles Ferguson², Tony Hyman¹, Robert G. Parton^{2,3} and Marino

4 Zerial¹

5

6 ¹Max Planck Institute of Molecular Cell Biology and Genetics, Pfotenhauerstraße 108, 01307 Dresden,

7 Germany.

8 ²Institute for Molecular Bioscience, University of Queensland, Brisbane, Queensland 4072, Australia.

9 ³Centre for Microscopy and Microanalysis, University of Queensland, Brisbane, Queensland 4072,
10 Australia.

11

12 To whom correspondence should be addressed.

13 Email: zerial@mpi-cbg.de

14

15

16

17

18

19

20 **Abstract**

21 Mitochondrial stress response is essential for cell survival, and damaged mitochondria are a
22 hallmark of neurodegenerative diseases. Thus, it is fundamental to understand how mitochondria relay
23 information within the cell. Here, by investigating mitochondrial-endosomal contact sites we made the
24 surprising observation that the small GTPase Rab5 translocates from early endosomes to mitochondria
25 upon oxidative stress. This process is reversible and accompanied by an increase in Rab5-positive
26 endosomes in contact with mitochondria. Interestingly, activation of Rab5 on mitochondria depends on
27 the Rab5-GEF ALS2/Alsin, encoded by a gene mutated in amyotrophic lateral sclerosis (ALS). Alsin-
28 deficient human induced pluripotent stem cell-derived spinal motor neurons are defective in relocating
29 Rab5 to mitochondria and display increased susceptibility to oxidative stress. These findings define a
30 novel pathway whereby Alsin catalyzes the assembly of the Rab5 endocytic machinery on
31 mitochondria. Defects in stress-sensing by endosomes could be crucial for mitochondrial quality
32 control during the onset of ALS.

33

34 **Introduction**

35 Mitochondria, the organelle for cellular metabolism and ATP production, play an essential role
36 in a number of other cellular processes such as calcium signaling, lipid synthesis and trafficking,
37 metabolite transport, apoptosis, and reactive oxygen species (ROS) production in the cell (Mesmin,
38 2016, Ott, Gogvadze et al., 2007, Rizzuto, De Stefani et al., 2012). Many of these processes necessitate
39 communication with other cellular compartments. For example, membrane contact sites (MCS)
40 between endoplasmic reticulum (ER) and mitochondria are important for Ca^{2+} and lipid transfer (de
41 Brito & Scorrano, 2008), mitochondria fission (Friedman, Lackner et al., 2011), and regulation of
42 apoptosis (Prudent, Zunino et al., 2015). Lipid droplets and peroxisomes interact with mitochondria to
43 regulate fatty acid oxidation (Cohen, Klug et al., 2014, Pu, Ha et al., 2011). Oxidized and damaged
44 proteins can be selectively delivered to peroxisomes and lysosomes via mitochondrial-derived vesicles
45 (Sugiura, McLelland et al., 2014). These examples demonstrate an extensive functional interplay
46 between organelles, either directly via MCS and/or indirectly via vesicular intermediates. However, the
47 underlying molecular mechanisms remain poorly understood and, in particular, the functional
48 relationship between mitochondria and the endocytic system is largely unexplored.

49 The endocytic pathway is responsible for maintaining cellular homeostasis by internalizing,
50 sorting, recycling and/or degrading distinct types of cargo molecules (Huotari & Helenius, 2011). Rab
51 GTPases serve as molecular signatures on endosomes, regulating their biogenesis and functions
52 (Pfeffer, 2017, Zerial & McBride, 2001, Zhen & Stenmark, 2015). Ligand-receptor complexes at the
53 plasma membrane (PM) are internalized into early endosomes (EE) marked by small GTPase Rab5,
54 followed by either recycling to the PM via Rab4 and Rab11-positive recycling endosomes (RE), or
55 routed to late endosomes (LE) and lysosomes for degradation. The latter process occurs via the
56 conversion of Rab5-positive EE into Rab7-positive LE (Rink, Ghigo et al., 2005, Sonnichsen, De

57 Renzis et al., 2000, Ullrich, Reinsch et al., 1996). Rab proteins can thus dynamically associate with the
58 membranes, conferring functional plasticity to organelles. On these endosomal membranes, Rab
59 proteins recruit a plethora of effectors for membrane tethering and fusion, cargo sorting and signaling
60 (Sorkin & von Zastrow, 2009, Stenmark, 2009, Zerial & McBride, 2001). For example, EEA1 is a
61 dimeric coiled-coiled Rab5 effector protein that tethers two vesicles to allow efficient fusion between
62 Rab5-harboring membranes (Murray, Jahnel et al., 2016, Ohya, Miaczynska et al., 2009). Other Rab5
63 effectors such as APPL1 are involved in regulating metabolic and inflammatory responses (Schenck,
64 Goto-Silva et al., 2008, Wen, Yang et al., 2010). Rab activation, and thus stabilization after
65 recruitment, on the membrane requires guanine nucleotide exchange factors (GEFs) (Blumer, Rey et
66 al., 2013). Rab5 GEFs constitute a family of VPS9 domain-containing proteins, including Rabex-5
67 (Horiuchi, Lippe et al., 1997), RME-6 (Sato, Sato et al., 2005), amyotrophic lateral sclerosis protein 2
68 (ALS2/Alsin) (Otomo, Hadano et al., 2003), and mammalian Ras and Rab interactor 1, 2, 3 (Rin1-3)
69 (Hu, Bliss et al., 2005). The rationale behind this complexity is that Rab5 must be specifically
70 regulated by different GEFs in space and time. In this respect, the function of many Rab5 GEFs
71 remains unclear.

72 Physical interactions between the endosomal machinery and mitochondria serve important
73 functions in cell homeostasis, repair and apoptosis. For example, transfer of iron (Das, Nag et al., 2016,
74 Sheftel, Zhang et al., 2007) and cholesterol (Charman, Kennedy et al., 2010) from endosomes to
75 mitochondria is mediated by physical interactions between the two organelles. Another classical
76 example of mitochondria-endolysosome interactions is autophagy. Autophagy is a clearance
77 mechanism whereby cells identify defective organelles following damage or stress, and eliminate them
78 via the formation of an autophagosome and subsequent fusion with lysosomes (Mizushima & Levine,
79 2010). The mechanism of degrading mitochondria has been termed macroautophagy or mitophagy.

80 Intriguingly, the expression of pro-apoptotic factors such as canonical BH3-only proteins drive Rab5-
81 and Rab7-positive endolysosomes into inner mitochondrial compartments via a pathway that appears
82 to differ from autophagy/mitophagy (Hamacher-Brady, Choe et al., 2014). Interestingly, our previous
83 conducted genome-wide RNAi screen of endocytosis (Collinet, Stoter et al., 2010) revealed that ~8%
84 of the hit genes had mitochondrial-related functions, pointing at hitherto unexplored molecular
85 connections between the endosomal system and mitochondria. This led us to hypothesize that other
86 mitochondrial functions may be regulated by endocytic components.

87 Here by exploring the interactions between EE and mitochondria, we unexpectedly found that
88 upon laser- or chemically-induced oxidative stress in mammalian cells, mitochondria outer membrane
89 permeabilization (MOMP) releases cytochrome c, and concomitantly, triggers the assembly of the
90 Rab5 machinery on mitochondria, in a process which is reversible and independent of mitophagy.
91 Remarkably, we found that the Rab5 GEF responsible for Rab5 activation is ALS2/Alsin, which is
92 necessary for efficient Rab5 recruitment to mitochondria. Our findings suggest that the Rab endocytic
93 machineries interact with mitochondria during oxidative stress as a cytoprotective mechanism, with
94 important implications for amyotrophic lateral sclerosis (ALS) and other neurodegenerative diseases.

95

96 **Results**

97 *Inter-organelle contacts between endosomes and mitochondria*

98 We first explored the potential physical link between the endosomal system and mitochondria
99 at steady state. HeLa cells stably expressing TagRFP-MTS (mitochondria targeting sequence)
100 (Takeuchi, Kim et al., 2013) were incubated with two types of endocytic cargo, Alexa-488-conjugated
101 transferrin (Tfn) or epidermal growth factor (EGF) for 10 min at 37°C, to visualize the
102 endocytic/recycling and degradative pathway, respectively. Cells were then fixed and imaged via
103 confocal microscopy. We observed a subset of endosomes that appeared to partially overlap with, or
104 were in close proximity to, mitochondria (Figure 1A,B). To avoid potential morphological changes
105 induced by the TagRFP-MTS overexpression, we also performed quantitative measurements in cells
106 stained for mitochondria with MitoTracker-Red CMXRos (Mito-Red) and labeled with Tfn-488 and
107 EGF-488 for 10 and 60 min at 37°C. All acquired images were subjected to chromatic shift correction,
108 deconvolution, and localization analysis (MotionTracking) based on subtraction of random
109 colocalization (Kalaidzidis, 2015). Tfn and EGF were efficiently internalized at 10 min, and further
110 sorted to distinct perinuclear compartments representing RE (Maxfield & McGraw, 2004) and
111 LE/lysosomes, respectively, at 60 min (Figure 1C). In both time points, Tfn-containing endosomes
112 consistently exhibited higher colocalization with Mito-Red (Figure 1D) compared to EGF-structures,
113 despite both having similar signal intensities (Figure 1E), suggesting that the interactions with
114 mitochondria may preferentially involve early/recycling endosomal structures.

115 Given that early endosomes are motile and omnipresent in the cytoplasm, we next asked
116 whether the observed physical proximity with mitochondria may reflect real MCS or be simply due to
117 random chance (Kalaidzidis, 2015). To further assess the interactions, we monitored the dynamics of
118 organelle contacts during early endocytic events by live-cell imaging. Cells were incubated with Tfn-

119 488 for 1 min to label EE and immediately imaged using a spinning disk confocal microscope. A
120 number of Tfn-containing endosomes and mitochondria labeled by TagRFP-MTS were observed in
121 close proximity, suggesting possible interactions (Video 1). Some endosomal vesicles remained in
122 close contact with mitochondria for 3-5 min and, interestingly, we could also observe interactions that
123 were followed by fission-like events (Video 2). Our data suggest that the occurrence of physical
124 contacts between EE and mitochondria observed in fixed and live cells may reflect *bona fide*, albeit
125 transient interactions, as suggested previously (Das, Nag et al., 2016, Sheftel, Zhang et al., 2007).

126
127 ***Acute mitochondrial stress recruits Rab5 and Rab5-positive endosomes to mitochondria***

128 Given the key role of mitochondria in sensing and responding to oxidative stress, we asked
129 whether acute perturbation on mitochondria may affect endosomes-mitochondria interactions. For this,
130 we used HeLa cells stably expressing GFP-Rab5 under its endogenous promoter with a bacterial
131 artificial chromosome (BAC) transgene (BAC GFP-Rab5) (Villasenor, Nonaka et al., 2015). These
132 cells were validated based on the lack of detectable alterations on endocytic trafficking. Live-cell
133 imaging of BAC GFP-Rab5 expressing RFP-MTS also confirmed the occurrence of Rab5-positive EE
134 (>200 nm) in close contact with mitochondria (Video 3).

135 To validate the results with the ectopically expressed mitochondrial marker, we tested
136 mitochondrial-selective dyes in our live-cell imaging. Unexpectedly, we found that photoirradiation in
137 cells labeled with Mito-Red not only robustly induced alterations in mitochondrial morphology but
138 also the appearance of GFP-Rab5 signals around mitochondria (Figure 2A). This is consistent with the
139 fact that certain rosamines and rhodamine-derived dyes used to assay mitochondrial functions possess
140 photosensitizing properties (Hsieh, Chu et al., 2015). Specifically, Mito-Red has been used to perturb
141 mitochondrial function (Minamikawa, Sriratana et al., 1999). Therefore, we hypothesized that the
142 change in Rab5 localization may be a consequence of alterations in mitochondrial function. Consistent

143 with previous reports, low exposure of Mito-Red labeled cells with a 561 nm laser ($\sim 5 \text{ J/cm}^2$) caused a
144 decrease in mitochondrial and an increase in cytoplasmic signal, indicative of MOMP, and
145 accompanied by a globular swelling of mitochondria within min (Figure 2A, Video 4). Remarkably,
146 laser treatment on Mito-Red labeled cells resulted in the translocation of GFP-Rab5 to mitochondria,
147 marked by increased colocalization with Mito-Red compared to the untreated (Figure 2B).
148 Furthermore, the frequency of GFP-Rab5 EE in close proximity to the stressed mitochondria increased
149 (Figure 2A, Post-laser arrowheads). This effect was specific to Mito-Red treatment, because cells
150 labeled with MitoTracker Green FM or transfected with RFP-MTS retained their tubular mitochondrial
151 structures under the same laser treatment and did not recruit GFP-Rab5 to the mitochondria (Figure 2–
152 figure supplement 1A,B, respectively). The presence GFP-Rab5 on mitochondria was independently
153 confirmed by staining with antibodies against Rab5 and the outer mitochondrial membrane (OMM)
154 protein TOM20 (Figure 2–figure supplement 1C).

155 Next, we examined the kinetics of GFP-Rab5 recruitment to Mito-Red labeled mitochondria
156 upon laser-induced stress. Time-lapse analysis revealed that the recruitment of Rab5 to rounded
157 mitochondria (Figure 2C, Pre- vs Post-laser) was visible within 5 min and reached its peak in signal
158 intensity at ~ 15 min post-laser treatment (Figure 2D,E; data correspond to the inset region of Figure
159 2C). The GFP-Rab5 ring-like signal persisted for >60 min (Figure 2–figure supplement 2, arrowheads).
160 In our time-lapse movies, we did not observe evidence of endosomal fusion with mitochondria (Figure
161 2E, Video 5), although we cannot exclude fusion with dim vesicles that may have escaped detection.
162 Our interpretation is that the bulk of Rab5 is recruited on mitochondria from the cytosolic pool. These
163 results suggest that upon acute oxidative stress, Rab5 translocates to mitochondria on the time-scale of
164 minutes.

165
166 ***Rab5 localizes to regions of mitochondria that are stressed***

167 We next asked if GFP-Rab5 translocation to mitochondria is a general response to the overall
168 cell stress or can be elicited locally on individual mitochondria. To test this, we photoirradiated a small
169 area of the cell labeled with Mito-Red (Figure 2F, Pre, inset) and monitored the GFP-Rab5 signal after
170 10 and 20 min. Despite the localized perturbation, the morphological alterations extended to most
171 mitochondria which changed from being tubular to rounded (Figure 2F, 10 min). This is consistent
172 with the fact that mitochondria form a dynamically interconnected network (Lackner, 2014, Wang, Du
173 et al., 2015) that appears to react to local damage as an ensemble. However, the recruitment of Rab5
174 was limited to only the laser-induced area (Figure 2F, 20 min, inset, arrowheads). Similar to Figure 2A,
175 distinct GFP-Rab5-positive endosomes contacting mitochondria became visible (Figure 2F, inset,
176 double arrowheads). These results suggest that Rab5 is recruited to mitochondria in response to
177 signal(s) originating from individually stressed mitochondria.

178
179 ***Membrane contacts between Rab5-positive mitochondria and endosomes***

180 The laser-induced stress to either an entire cell or a localized region led to the appearance of
181 Rab5-positive endosomes in close proximity to the swollen mitochondria (Figure 2A,F, arrowheads).
182 By live-cell imaging, these endosomes also appeared to dock stably onto mitochondria (Video 6, boxed
183 regions, Video 7). However, due to the diffraction limit of standard light microscopy, we could not
184 resolve distances that are closer than 200 nm and endosomes that are <200 nm in diameter. To confirm
185 that these are indeed organelle contacts, we complemented our study by correlative light and electron
186 microscopy (CLEM) in order to obtain ultrastructural details. We designed our experimental setup to 1)
187 perform live-imaging of an entire cell, 2) visualize the translocation of GFP-Rab5 and GFP-Rab5-
188 positive endosomes onto mitochondria upon laser-induced stress, and 3) re-image the same cell by
189 serial section transmission electron microscopy (TEM) (Figure 3A). GFP-Rab5 cells labeled with
190 Mito-Red were plated on gridded culture dishes, laser-treated and imaged live on the spinning disk

191 confocal microscope. Upon mitochondrial rounding, cells were immediately fixed and re-imaged to
192 assess organellar morphology following fixation. The fluorescent images showed many distinct GFP-
193 Rab5-positive puncta in close proximity to mitochondria (Figure 3A). Samples were then processed for
194 serial section TEM, and an inset area tracked by live-cell imaging (Figure 3B, red arrowhead) was re-
195 located in the thin sections by both nuclear membrane (Figure 3B, dotted line) and mitochondria
196 (Figure 3B, red stars) acting as fiducial markers. TEM images from three different serial sections of the
197 inset area revealed that the GFP-Rab5-positive structure corresponds to a tubular-cisternal structure
198 that is approximately 400 nm in diameter, with the typical morphology of an early endosome (Figure
199 3C, green). Serial section analysis showed that the endosomal membrane was in very close contact (<5
200 nm) with the adjacent mitochondrion of a diameter of $\sim 1.5 \mu\text{m}$ (Figure 3C, red), which showed few
201 cristae. The tomogram showed the presence of membrane contact sites between the rounded
202 mitochondrion and a cisternal structure that could correspond to the ER, but did not reveal the presence
203 of double or multiple membranes indicative of mitophagy (Youle & Narendra, 2011). Our data suggest
204 that upon mitochondrial stress, two events involving early endosomes and mitochondria occur: 1) Rab5
205 translocates to mitochondria and 2) endosomes and mitochondria engage in membrane contacts.

206
207 ***The recruitment of Rab5 to mitochondria is not due to mitophagy***

208 Following mitochondrial stress, both the fast kinetics (min) of Rab5 recruitment on the rounded
209 mitochondria and the absence of wrapped double-membrane structures argue against mitophagy
210 (Narendra, Tanaka et al., 2008, Novak, Kirkin et al., 2010). We searched for additional evidence to
211 rule out this mechanism. Mitophagy requires the E3 ubiquitin ligase Parkin (Narendra et al., 2008),
212 which is normally located in the cytosol but recruited to damaged mitochondria, followed by the
213 formation of LC3-positive autophagosomes and fusion with Lamp1-positive lysosomes in a process
214 that occurs in hours (hr) to days (Dolman, Chambers et al., 2013). To test whether the swollen

215 mitochondria observed in our system undergo this process, we examined the localization of these
216 markers. We first labeled BAC GFP-Rab5 cells with Mito-Red in order to image mitochondria and
217 endosomes at steady state (Figure 4A,C,E,G, Untreated) prior to triggering laser-induced stress. Upon
218 fixation, cells were immunostained with specific antibodies to detect endogenous LC3, Lamp1, and
219 Parkin. The cells were seeded on a gridded dish in order to re-locate the same cells following the
220 immunostaining. This allowed us to assess changes to the localization of the markers as a result of
221 stress when compared to neighboring untreated cells (Figure 4–figure supplement 1). Cells were then
222 incubated for 60 min at 37°C in order to maximize the time window that these markers might be
223 recruited following GFP-Rab5 translocation to mitochondria. In all laser-induced cells, GFP-Rab5 was
224 specifically enriched around mitochondria when compared to the untreated (Figure 4B,D,F). Although
225 we observed a marginal increase in LC3 and Lamp1 colocalization with Mito-Red in stress-induced
226 cells, the signals were mostly concentrated near the perinuclear region (Figure 4B,D,I). On the other
227 hand, Parkin remained mostly cytoplasmic and did not show enrichment around mitochondria in stress-
228 induced cells (Figure 4F,I).

229 As an additional validation of the immunostaining result, we also tested all three markers in
230 HeLa BAC cell lines expressing GFP-tagged LC3, Lamp1, and Parkin by live-cell imaging (Figure 4–
231 figure supplement 2). Following laser irradiation, cells were monitored live for 60 min. Similar to the
232 endogenous LC3 and Lamp1 staining, a fraction of the puncta was enriched in the perinuclear region,
233 overlapping with small fragmented mitochondria, but not with the rest of the mitochondria (Figure 4–
234 figure supplement 2A,B), suggesting that a low level of autophagy is activated. The GFP-Parkin
235 signals were mostly cytoplasmic in untreated cells but showed a few GFP-Parkin-positive ring-like
236 structures around small fragmented mitochondria, whereas most were devoid of signal in the laser-
237 induced condition (Figure 4–figure supplement 2C, arrowheads). Even after 3 hr post treatment, we

238 observed no significant increase in the number of GFP-Parkin mitochondria (data not shown). The
239 GFP-Parkin ring-like recruitment to these small fragmented mitochondria could be a result of over-
240 expression, inducing some level of mitophagy (Rana, Rera et al., 2013). Nevertheless, similar to
241 endogenous staining, Parkin was not strongly recruited to the majority of mitochondria. Altogether, the
242 fast kinetics of Rab5 recruitment to stressed mitochondria (<10 min), the absence of a double
243 membranous structure (Figure 3C), and the lack of significant Parkin, LC3 and Lamp1 recruitment
244 argue for a mechanism distinct from autophagy and mitophagy.

245
246 *Apoptotic signaling is partially activated in laser-induced oxidative stress*

247 The low level of autophagic and mitophagic response raise the question of whether apoptosis is
248 involved. Apoptosis is a programmed cell death pathway which occurs via one of two signaling
249 cascades termed intrinsic and extrinsic pathways (Tait & Green, 2010). The intrinsic pathway is
250 initiated through the activation of the Bax/Bak-mediated MOMP, which leads to the release of
251 cytochrome c to activate effector caspases (Tait & Green, 2010). Because photoirradiation with Mito-
252 Red engenders oxidative stress in mitochondria (Hsieh et al., 2015), we also examined the localization
253 of endogenous Bax via immunostaining. At steady state, Bax signals were visible as cytoplasmic
254 puncta (Figure 4G). Upon laser-induced stress, we observed increased Bax puncta around
255 mitochondria compared to the untreated (Figure 4H,I). As a positive control for the specificity of the
256 antibody, we treated cells with 10 μ M protonophore carbonyl cyanide m-chlorophenyl hydrazone
257 (CCCP), which has been shown to cause Bax translocation to mitochondria (Mikhailov, Mikhailova et
258 al., 2001, Saikumar, Dong et al., 1998). Indeed, cells treated with CCCP exhibited higher Bax
259 fluorescence intensity and colocalization with Mito-Red compared to control cells (Figure 4—figure
260 supplement 3).

261 The observed enrichment of Bax on mitochondria upon laser-induced stress led us to ask
262 whether artificially activating apoptosis would also drive Rab5 translocation to mitochondria. One
263 method of triggering mitochondrial-associated apoptosis is the over-expression of the truncated BH3
264 interacting death domain agonist (tBid), which is a potent inducer of apoptosis by activating Bax
265 and/or self-oligomerization on mitochondria (Grinberg, Sarig et al., 2002). To this end, we infected
266 BAC GFP-Rab5 cells with an adenoviral vector expressing tBid (Ad-tBid) for 12 hr at 37°C followed
267 by TOM20 immunostaining. We found a strong enrichment of GFP-Rab5 on mitochondria only in
268 cells infected with Ad-tBid but not in Ad-control cells (Figure 4—figure supplement 4). Our results
269 suggest a mechanism of Rab5 translocation to mitochondria in response to apoptotic signals.

270
271 ***Hydrogen peroxide triggers Rab5 translocation to mitochondria and affects mitochondrial***
272 ***respiration without disrupting membrane potential***

273 What could be the signal that drives Rab5 recruitment? Several possible scenarios such as
274 morphological changes to mitochondria and/or release of mitochondrial-derived factor(s) may account
275 for this. Morphological changes such as matrix condensation or swelling of mitochondria are often
276 associated with MOMP by Bax activation, cytochrome c release and subsequent activation of caspases
277 (Gottlieb, Armour et al., 2003). However, this is not a prerequisite. For example, the mitochondrial
278 uncoupler CCCP causes mitochondrial swelling and rounding but without immediate cytochrome c
279 release or cell death (Gao, Pu et al., 2001, Lim, Minamikawa et al., 2001). On the other hand,
280 hydrogen peroxide (H₂O₂) induces mitochondrial rounding associated with increased Bax expression
281 (Gutierrez-Venegas, Guadarrama-Solis et al., 2015), cytochrome c release and caspase activation
282 (Gutierrez-Venegas et al., 2015, Takeyama, Miki et al., 2002). For these reasons, we first investigated
283 the effect of CCCP and H₂O₂ on Rab5 localization. Whereas mitochondria were mostly tubular in
284 control cells (Figure 5A,B, top panels), the exposure of cells to either CCCP or H₂O₂ for 2 hr resulted

285 in mitochondrial rounding and fragmentation (Figure 5A,B, bottom panels), as previously reported
286 (Narendra et al., 2008, Pletjushkina, Lyamzaev et al., 2006). Interestingly, CCCP did not cause Rab5
287 enrichment on mitochondria, which was only observed in H₂O₂-treated cells (Figure 5A,B,
288 arrowheads), quantified as colocalization with Mito-Red (Figure 5C,D). Consistent with previous
289 findings, we found that the release of cytochrome c into the cytosol was upregulated in H₂O₂-treated,
290 but not in CCCP-treated cells (Figure 5E). Since cytochrome c is a known factor for activating
291 caspase-dependent programmed cell death, we also assessed the activity of caspase 3/7 via a 4-amino
292 acid peptide (DEVD) conjugated to a DNA-binding dye. Cleavage of the DEVD peptide by caspase
293 3/7 releases the DNA-binding fragment, yielding a fluorescent signal. Using flow cytometry, we
294 detected ~62% of cells showing strong fluorescent signal in H₂O₂-treated cells, and merely ~0.6% and
295 ~6.2% in control and CCCP-treated cells, respectively. As additional controls of the treatment, we
296 showed that only CCCP, but not H₂O₂, resulted in the recruitment of GFP-Parkin as well as
297 endogenous Parkin on mitochondria (Figure 5–figure supplement 1A,B).

298 Given the primary role of mitochondria in cellular metabolism, we asked whether the observed
299 differences between CCCP and H₂O₂ could be related to altered mitochondrial respiration. To test this,
300 we measured the oxygen consumption rate (OCR) in live HeLa cells grown in the presence of
301 galactose in order to force cells to rely primarily on oxidative phosphorylation as opposed to glycolysis
302 (Aguer, Gambarotta et al., 2011). Upon the addition of CCCP, a sharp increase in OCR was recorded
303 compared to the media control (Figure 5G, purple vs orange curve). This is because CCCP causes the
304 collapse of the proton gradient and the disruption of the mitochondrial membrane potential. As a result,
305 electrons flow unhindered through the electron transport chain, boosting the OCR. In contrast,
306 injection of H₂O₂ resulted in an initially sharp decline in OCR, but quickly returned to its earlier steady
307 state within 20 min (Figure 5G, green curve), suggesting that the effect on OCR is reversible. The

308 decrease in respiration rate by H₂O₂ was similarly reported in intact cardiac mitochondria, in which α-
309 ketoglutarate was used as a respiratory substrate (Nulton-Persson & Szweda, 2001). Altogether, our
310 data show that, in addition to activating caspase-dependent apoptotic program, H₂O₂ also induces the
311 translocation of Rab5 to mitochondria without disrupting the membrane potential.

312
313 ***Hydrogen peroxide-induced stress triggers Rab5 translocation from EE to mitochondria, increases***
314 ***early endosomal-mitochondrial contacts, and interferes with transferrin uptake***

315 Given the key role of Rab5 in the biogenesis of the endosomal system (Zeigerer, Gilleron et al.,
316 2012, Zerial & McBride, 2001), the translocation of Rab5 to mitochondria upon oxidative stress by
317 H₂O₂ led us to investigate the connection between endocytosis and oxidative stress. Our live-cell
318 imaging data (Figure 2,3) argue that GFP-Rab5 is not delivered to mitochondria by fusion with EE.
319 Rather, it may be released from EE and recruited to mitochondria via a cytosolic intermediate. To test
320 this, we collected the total membrane (M) and cytosolic (C) fractions by subcellular fractionation from
321 HeLa cells treated with/out H₂O₂ and immunoblotted for Rab5, the endosomal tether Rab5 effector
322 EEA1, GAPDH (as cytosolic marker), and TOM20 (a mitochondrial marker) (Figure 6A). It was
323 previously shown that H₂O₂-induced stress causes increased Rab5-GDI complex in BHK cells (Cavalli,
324 Vilbois et al., 2001). Consistent with this, upon 1 hr H₂O₂ treatment, we detected a ~0.5-fold increase
325 in the amount of Rab5 in the cytosolic fraction compared to the control (Figure 6A, lane 2,4),
326 supporting the view that the cytosolic pool increases at the expense of the membrane-associated pool.
327 The cytosolic levels of Rab5 then decreased at 2 hr time point (Figure 6A, lane 4,6, Figure 6B). We
328 also detected an increase in the EEA1 pool to the cytosol in the long exposure upon H₂O₂ treatment
329 (Figure 6A, right blot). Since Rab5 in the M fraction includes both the EE and mitochondrial pool, we
330 specifically measured the EE-associated Rab5 by estimating the colocalization of Rab5 with EEA1 by
331 confocal immunofluorescence microscopy. We found a marked (~35%) decrease in the colocalization

332 in H₂O₂-treated compared to untreated cells (Figure 6C). Altogether, our results suggest that oxidative
333 stress induces the solubilization of a fraction of Rab5 from the endosomal membrane into the cytosol
334 and its translocation to the mitochondrial membrane.

335 The partial dissociation of Rab5 and EEA1 from the endosomal membrane suggests that
336 endocytic trafficking may be affected. To test this, we stimulated HeLa cells with Alexa-647 Tfn
337 continuously for 5 min at 37°C. In the absence of H₂O₂, transferrin was efficiently internalized into
338 endosomes (Figure 6D, Untreated). In contrast, cells pre-treated with H₂O₂ for 10 min showed a severe
339 block in Tfn uptake with an accumulation of Tfn signal on the cell surface (Figure 6D,E), confirming
340 the inhibition of endocytic uptake.

341 In the laser-induced stress conditions, we observed a high occurrence of EE contacting stressed
342 mitochondria (Figure 2A,F,Figure 3), and these interactions appeared to be specific to EE (Figure 1).
343 The effects by H₂O₂ prompted us to further probe whether differential interactions exist between
344 mitochondria and Tfn- vs. EGF-positive endosomes. To test this, HeLa cells stained with MitoRed
345 were continuously labeled with either Tfn-488 or EGF-488 for 10 min at 37°C and then incubated for
346 50 min with/out H₂O₂. There was a significant increase in the colocalization between Mito-Red and
347 both Tfn-488 and EGF-488 in H₂O₂-treated compared to non-treated cells (Figure 1C,D). Intriguingly,
348 we also found an increase in the total signal intensity in H₂O₂ conditions (Figure 1E), in which Tfn
349 signals accumulated more prominently in the perinuclear region (typical of RE) whereas EGF was
350 more evenly distributed compared to untreated (Figure 1C). Increased colocalization with H₂O₂ is
351 likely attributed to a block in recycling of Tfn (as uptake is inhibited) and sorting of EGF to
352 LE/lysosome, thereby resulting in cargo accumulation in EE.

353 Altogether, our data suggest that oxidative stress induced by laser irradiation or H₂O₂ leads to
354 Rab5 translocation from EE to mitochondria, increased EE-mitochondrial MCS, and a defect in
355 endosomal sorting.

356
357 ***Stress-induced Rab5 translocation to mitochondria blocks cytochrome c release***

358 By live-cell imaging, we found that mitochondria respond to H₂O₂ treatment with different
359 kinetics within a cell (Video 8). Distinct regions of the mitochondrial network were more prone to
360 rounding and membrane permeabilization than others, as revealed by the differential loss of Mito-Red
361 during H₂O₂ treatment (Figure 7A, inset image). Regions containing stressed rounded mitochondria
362 correlated exclusively with the Rab5 ring-like recruitment (Figure 7A, inset image, arrowheads),
363 suggesting that Rab5 may be involved in either facilitating or preventing the apoptotic process.
364 Therefore, we asked whether Rab5 plays a role in regulating cytochrome c release. For these
365 experiments, we transiently over-expressed GFP-Rab5 (or GFP as control) in HeLa cells and measured
366 the amount of cytosolic cytochrome c at different time points after incubation with H₂O₂. We found a
367 significant delay in the cytochrome c release from mitochondria in GFP-Rab5 over-expressing cells
368 compared to control cells (Figure 7B,C). Our results suggest that Rab5 plays a protective role in
369 mitochondrial-induced apoptosis by down-regulating the release of pro-apoptotic factor(s) to the
370 cytosol.

371
372 ***Rab5 enrichment on mitochondria is reversible***

373 We reasoned that if the translocation of Rab5 to mitochondria induced by oxidative stress is a
374 pro-survival response by lowering the apoptotic potential, then the process should be reversible when
375 stress is removed and mitochondria may recover their normal state. The fast recovery rate of
376 mitochondrial respiration following H₂O₂ injection (Figure 5E) also supports this prediction. We

377 initially tested a range of H₂O₂ concentrations (100 μM to 1 mM) and incubation times (2 to 24 hr), in
378 order to find an optimal balance between a measurable level of Rab5 translocation to mitochondria and
379 minimal cell death. We found that concentrations up to 500 μM did not cause a noticeable cell
380 rounding by 2 hr (data not shown). Therefore, we pre-incubated cells with 250 μM H₂O₂ over a period
381 of 24 hr and quantitatively measured TOM20 levels and Rab5-mitochondria colocalization as a means
382 to assess mitochondrial mass and interaction dynamics. Cells were incubated in the presence or
383 absence of H₂O₂ for 6, 12 and 24 hr, and either lysed for Western blot analysis or fixed for
384 immunostaining. Interestingly, we found that the levels of TOM20 started to increase after 6 hr,
385 suggesting that the mitochondrial mass increased (Figure 8A, left panels). In immunostained cells, we
386 found that the colocalization between endogenous TOM20 and Rab5 (Figure 8B) peaked at 6 hr and
387 started to taper off after 12 hr (Figure 8C). Decreased colocalization correlated with increased TOM20
388 protein levels (Figure 8A). Remarkably, the removal of H₂O₂ at 12 hr followed by an additional 12 hr
389 incubation in complete medium not only fully restored the morphology of mitochondria from rounded
390 to tubular (Figure 8B, bottom panel), but also returned TOM20:Rab5 colocalization to steady state
391 levels (Figure 8C). The response was dose-dependent as cells exposed to 500 μM H₂O₂ showed
392 arrested TOM20 levels and were unable to be rescued despite H₂O₂ removal at 12 hr (Figure 8A, right
393 panels). Our data show that Rab5 translocation to mitochondria induced by oxidative stress is a
394 reversible and protective process responding to apoptotic signals via the regulation of mitochondria.

395
396 ***Rab5 enrichment on mitochondria is accompanied by specific effector recruitment***

397 Because Rab5 translocates from EE to mitochondria with a consequent reduction in endocytic
398 uptake, we next asked whether the endosomal Rab5 effectors are also recruited to mitochondria. We
399 systematically assessed the localization of various endosomal effectors such as Rabenosyn-5, EEA1,
400 APPL1 and APPL2 in BAC GFP-Rab5 HeLa cells labeled with Mito-Red via immunostaining by pair-

401 wise combinations. We deliberately chose to detect the endogenous because the tagged proteins often
402 severely perturb the endosomal system, as assessed by quantitative endocytic trafficking (Kalaidzidis,
403 Miaczynska et al., 2015). Specific antibodies were first tested in untreated control cells, which showed
404 significant levels of colocalization with GFP-Rab5 (Figure 9–figure supplement 1). Upon laser-
405 induced stress, the appearance of GFP-Rab5 rings around mitochondria provided an immediate visual
406 cue and served as a positive control. Cells were fixed after 30 min incubation post-laser treatment. Of
407 the tested effectors, we detected a strong enrichment of Rabenosyn-5, but not EEA1, on mitochondria
408 in the same cell (Figure 9A,C). Neither APPL1 nor APPL2 showed enrichment around mitochondria,
409 despite a robust Rab5 recruitment (Figure 9B,C). Unlike Rabenosyn-5, EEA1, APPL1 and APPL2
410 remained well distributed in endosomal-like vesicles in both treated and untreated cells (Figure 9A,B,
411 Figure 9–figure supplement 1B,C,D). As Rabenosyn-5 and EEA1 are recruited to endosomes via both
412 Rab5 and PI(3)P-binding FYVE motifs (Nielsen, Christoforidis et al., 2000), we asked whether
413 phosphatidylinositol 3-phosphate (PI(3)P) was present on mitochondria in our stress conditions. To test
414 this, we over-expressed the PI(3)P probe GFP-2xFYVE^{Hrs} (Gillooly, Morrow et al., 2000) in HeLa
415 cells and monitored GFP signals in live cells upon laser-induced stress. Fluorescence signals were
416 present as vesicle-like puncta (Figure 9–figure supplement 2, 0 min), as previously reported (Gillooly,
417 Morrow et al., 2000). After 60 min, stressed and swollen mitochondria were observed, but these were
418 completely devoid of GFP signals, which remained on vesicle-like puncta (Figure 9–figure supplement
419 2, 60 min).

420 To corroborate the immunostaining data with an independent method, we also tested the effect
421 of H₂O₂ on Rab5 and Rab5 effectors in association with mitochondria by subcellular fractionation. We
422 isolated cytosolic (C) and mitochondrial fractions (Mito) via differential centrifugation and probed
423 them with different effector antibodies by Western blot (Figure 9D). Consistent with our

424 immunostaining results, Rab5 and Rabenosyn-5, but not EEA1 and APPL1/2, were found to be
425 specifically enriched in the mitochondrial fraction (marked by TOM20) treated with H₂O₂ compared to
426 non-treated (Figure 9D, lane 2,4).

427 Altogether, our findings reveal a selective mechanism of Rab5 translocation and activation on
428 mitochondria in the absence of PI(3)P.

429
430 ***The Rab5 GEF Alsin localizes to mitochondria upon stress induction***

431 Translocation and recruitment of effectors imply that Rab5 must be activated on the
432 mitochondrial membrane. Activation of Rab GTPases on organelle membranes depends on a family of
433 GEFs (Blumer et al., 2013, Pfeffer, 2013, Zerial & McBride, 2001, Zhen & Stenmark, 2015). We first
434 examined the localization of Rabex-5, a known GEF of Rab5 on the endosomal membrane, by
435 immunostaining in BAC GFP-Rab5 cells. For reasons described above, we visualized the endogenous
436 protein because tagged Rabex-5 constructs proved not to be functional as judged by their perturbations
437 on the endosomal system (Kalaidzidis and Zerial, unpublished data). The formation of GFP-Rab5 rings
438 upon laser treatment served as a positive control. Despite a modest enrichment on mitochondria upon
439 laser-induced stress, endogenous Rabex-5 remained mostly cytosolic and on cytoplasmic puncta
440 (Figure 10A), consistent with its endosomal localization (Figure 10–figure supplement 1A).

441 The localization pattern of Rabex-5 led us to hypothesize that another GEF might be principally
442 involved. We turned our attention to Alsin based on several lines of evidence. Alsin is the gene product
443 of ALS2, which is mutated in multiple neurodegenerative disorders such as juvenile amyotrophic
444 lateral sclerosis (ALS), juvenile primary lateral sclerosis (JPLS), and infantile-onset ascending
445 hereditary spastic paralysis (IAHSP). Alsin comprises three GEF domains: 1) a RCC1-like GEF
446 domain for Ran GTPase, 2) a DH-PH domain for Rho GTPase, and 3) a C-terminal VPS9 domain for
447 Rab5 (Topp, Carney et al., 2005) (Figure 10–figure supplement 1B). Functional studies in ALS mouse

448 models have associated Alsin with neuronal survival (Kanekura, Hashimoto et al., 2004, Panzeri, De
449 Palma et al., 2006) and endolysosomal trafficking (Hadano, Mitsui et al., 2016, Hadano, Otomo et al.,
450 2010). Moreover, corticospinal motor neuron (CSMN) in Alsin KO mice display selective defects in
451 mitochondrial morphology (Gautam, Jara et al., 2016). At steady state, Alsin localized to vesicular
452 structures, showing partial overlap with Rab5 (Figure 10–figure supplement 1C), consistent with the
453 reported localization of Alsin (Kanekura et al., 2004, Topp, Gray et al., 2004). However, after laser
454 treatment, Alsin exhibited a strong and uniform staining around mitochondria (Figure 10B), where it
455 showed significant colocalization with GFP-Rab5 and Mito-Red (Figure 10C).

456 The spatial and functional connection between Alsin and Rab5 suggest that Alsin may also be
457 implicated in stress-induced response on mitochondria. We tested this idea by over-expressing either
458 Alsin or WT Rab5 in HeLa cells and found that both prevented caspase 3/7 activation as revealed by
459 the weak fluorescence signals (due to the lack of cleavage on the DEVD-conjugated DNA-binding dye)
460 compared to control cells, when challenged with H₂O₂ (Figure 10–figure supplement 2A,B). Our
461 results point to Alsin as a candidate GEF for activating Rab5 on mitochondria upon stress induction.

462
463 ***Alsin regulates mitochondrial apoptotic signaling and is required for efficient Rab5 targeting to***
464 ***mitochondria***

465 Several mouse models have been generated for the studies on Alsin. However, these models
466 have failed to recapitulate the phenotypes observed in human patients (Cai, Shim et al., 2008). It has
467 recently been reported that the absence of Alsin appears to specifically affect the health of
468 corticospinal motor neurons (Gautam et al., 2016). Therefore, in order to directly probe the role of
469 Alsin in a more physiological background without compromising our ability for genetic and chemical
470 manipulations, we generated Alsin CRISPR knockout cells in human induced pluripotent stem cells
471 (iPSCs). We confirmed the deletion of the Alsin gene by sequencing (not shown) and RT-PCR, and the

472 encoded protein by Western blot (Figure 11–figure supplement 1A,B). We were then able to
473 differentiate both WT and mutant (*Alsin*^{-/-}) iPSCs into spinal motor neurons (iPSC-sMNs) using a
474 previously reported protocol (Reinhardt, Glatza et al., 2013). In short, we induced neural progenitor
475 cells (NPC) through embryonic bodies formation by growing iPSC in a medium supplemented with
476 transforming growth factor- β (TGF- β) and bone morphogen protein (BMP) small molecule inhibitors
477 (SB431542 and dorsomorphin, respectively), and WNT and Sonic Hedgehog signaling activators
478 (CHIR99021 and PMA, respectively). Differentiation and maturation stages were achieved by
479 culturing cells in retinoic acid (RA), cAMP, and neurotrophic factors (BDNF and GDNF) (Figure 11A).
480 As a quality control, high expression of pluripotency markers such as Oct4 and Lin28 were observed in
481 our iPSCs as well as Nestin, Sox2 and Pax6 expression in our neuro-progenitor cells (NPCs) (Figure
482 11–figure supplement 1C). Differentiation into mature spinal motor neurons was validated by the
483 expression of choline acetyltransferase (ChAT), HB9, and Islet-1 (ISL1) (Figure 11–figure supplement
484 1D,E). These cells showed extensive axonal network as revealed by the MAP2 staining (Figure 11–
485 figure supplement 1E). Finally, mature spinal motor neurons were re-stained for the expression of
486 *Alsin* in both WT and *Alsin*^{-/-} cells (Figure 11–figure supplement 1F).

487 We first examined the steady state localization of Rab5 and morphology of mitochondria by
488 immunostaining for endogenous Rab5 and TOM20. Similar to hippocampal neurons (de Hoop, Huber
489 et al., 1994), Rab5 was ubiquitously present on endosomal-like vesicles in the soma, dendrites and
490 axon in iPSC-sMNs. The mitochondrial network in iPSC-sMNs was less tubular, and contained more
491 numerous and smaller rounded mitochondria than those in HeLa cells (Figure 11B, Ctrl). Next, we
492 tested whether iPSC-sMNs would exhibit the same mitochondrial response to oxidative stress as
493 observed in HeLa cells. Noticeably, we found iPSC-sMNs to be more susceptible to detachment and
494 cell rounding than HeLa cells when challenged with 250 μ M H₂O₂ for 2 hr under the same conditions

495 (data not shown). We thus lowered the H₂O₂ concentration to 100 μM such that no immediate cell
496 detachment nor rounding were observed during the treatment. We then examined the morphology of
497 mitochondria, the association of Rab5 with mitochondria, and the release of cytochrome c into the
498 cytosol. At steady state, we did not observe significant alterations in mitochondria morphology in both
499 WT and *Alsin*^{-/-} iPSC-sMNs. However, WT iPSC-sMNs challenged with H₂O₂ showed a robust
500 enrichment of Rab5 on mitochondria, but not in *Alsin*^{-/-} iPSC-sMNs (Figure 11B, H₂O₂).

501 To corroborate these results, we also performed subcellular fractionation of iPSC-sMNs. In
502 control cells, endogenous Rab5 was detected primarily in the cytosolic fraction and minimally in the
503 mitochondrial fraction (Figure 11C, lane 1,2,5,6). On the other hand, cells challenged with H₂O₂
504 showed a strong enrichment of Rab5 co-fractionating with the mitochondrial fraction in WT iPSC-
505 sMNs, but only weakly in *Alsin*^{-/-} iPSC-sMNs (Figure 11C, lane 3,7). The lack of Rab5 enrichment in
506 *Alsin*^{-/-} cells also correlated with a greater susceptibility to H₂O₂-induced apoptotic signaling, as
507 assessed by the rapid release of cytochrome c into the cytosol within 1 hr and subsequent accumulation,
508 when compared to WT cells (Figure 11D). Collectively, our findings demonstrate that *Alsin* is a key
509 regulator for recruiting Rab5 to mitochondria, which altogether, impart a cytoprotective function for
510 cells against oxidative stress.

511

512 **Discussion:**

513 We discovered a novel cytoprotective mechanism during oxidative stress entailing the
514 translocation of Rab5 from EE to mitochondria. Interestingly, the activation of Rab5 requires Alsin,
515 which has been implicated in early onset ALS. Our results provide an unexpected mechanistic link
516 between the endosomal system and mitochondria that could be of primary importance for
517 understanding the mechanistic cause of ALS and other neurodegenerative diseases.

518 Different nutrient or environmental perturbations can affect mitochondria morphology and
519 metabolic activities such as oxidative phosphorylation and programmed cell death (Galloway & Yoon,
520 2013). Mitochondria can elicit adaptive responses to oxidative stress that may lead to hypoxia
521 adaptation, inflammation, or programmed cell death (Sena & Chandel, 2012). Our findings suggest
522 that the endocytic system is a primary responder to mitochondria under oxidative stress. Laser- or
523 exogenous ROS (e.g. H₂O₂)-induced damage causes MOMP, mitochondrial swelling, and release of
524 cytochrome c, leading to caspase activation and apoptosis. Under these conditions, the endosomal
525 system appears to rapidly respond to damaged mitochondria through a rescue pathway, which results
526 in the recruitment of Alsin and Rab5 to mitochondria, inhibition of cytochrome c release, decrease in
527 mitochondrial oxygen consumption and hence, increased overall cell viability (Figure 12). In the
528 course of this study, a mitochondrial clearance mechanism was reported where Rab5-positive EE
529 sequester mitochondria via the ESCRT machinery when cells are treated with the proton uncoupler
530 FCCP (Hammerling, Najor et al., 2017), an analog of CCCP. Our mechanism appears to be distinct
531 from this as well as the canonical autophagic/mitophagic mechanisms. First, we did not observe the
532 engulfment of mitochondria into Rab5-positive EE but rather, the recruitment of Alsin, Rab5, and
533 Rabenosyn-5 on mitochondria, as well as an increase in early endosomal-mitochondrial MCS in
534 response to stress. This is also distinct from the intra-mitochondrial recruitment of Rab5 and endo-

535 lysosomes upon over-expression of the apoptotic factors (Hamacher-Brady et al., 2014). Second, we
536 did not observe engulfing membraneous structures around stressed mitochondria nor upon CCCP
537 treatment. One explanation could be the use of different cell types and the lower concentration of
538 CCCP employed in our experiments. Third, the recruitment of Rab5 to damaged mitochondria occurs
539 rapidly, i.e. within min, well preceding any autophagic components that we analyzed in this study. We
540 found that autophagy is restricted to only a subset of small mitochondrial fragments that are LC3⁺
541 whereas the majority are devoid of known autophagic markers such as Parkin, LC3 and Lamp1. We
542 could not rule out that mitochondrial clearance mechanism may still be activated at a later time.
543 However, our data with H₂O₂ show that the mechanism described here is reversible (Figure 8) and
544 argue for a mitochondrial-protective role rather than a degradative process. In fact, the reversal and
545 recovery of cells from late-stage apoptosis (i.e. following cytochrome c release and caspase activation)
546 have recently been reported in multiple cells lines including HeLa cells and brain cells in a process
547 called “anastasis” (Sun, Guzman et al., 2017, Tang, Tang et al., 2012), suggesting that this may be a
548 general mechanism to cope with cellular stress. We attempted to track the fate of individually damaged
549 mitochondria in a localized region after laser treatment (data not shown), but the continuous
550 photoirradiation required to achieve a high spatio-temporal resolution also led to a quick decrease in
551 MitoTracker Red signal and undesirable additional stress to the cell over time, preventing us from
552 determining its precise outcome. The loss of Mito-Red signal is likely due to MOMP, as evident by the
553 release of cytochrome c, and not a result of mitochondrial clearance because the outer mitochondrial
554 membrane can be stained by TOM20 and visualized by the presence of Rab5 ring-like formation.

555 Which molecular mechanism is responsible for the dissociation of Rab5 from EE and its
556 recruitment to mitochondria? On EE, the levels of Rab5 depend on the equilibrium between the
557 cytosolic pool of Rab5 complexed to Rab GDI and the membrane-associated pool sustained by the

558 Rabex-5/Rabaptin-5 complex and a plethora of Rab5 effectors (Del Conte-Zerial, Bruschi et al., 2008,
559 Lippe, Miaczynska et al., 2001, Zerial & McBride, 2001, Zhang, Zhang et al., 2014). Prior studies have
560 shown that such equilibrium, and consequently endocytic trafficking, is adaptive to stress and
561 apoptotic signal. For example, Rabaptin-5 is selectively cleaved by caspase-3 during apoptosis, thus
562 affecting its interaction with Rab5 and reducing the overall endocytic capacity (Cosulich, Horiuchi et
563 al., 1997, Swanton, Bishop et al., 1999). The activation of p38 MAPK by H₂O₂ also stimulates the
564 formation of the GDI:Rab5 complex, thus favoring the extraction of Rab5 from the early endosomal
565 membrane (Cavalli et al., 2001). In addition, p38 MAPK modulates the endosomal function via
566 phosphorylation and membrane association of Rab5 effectors (Mace, Miaczynska et al., 2005). Such a
567 mechanism may account for the mobilization of Rab5 from the endosomal membrane, which is
568 suggested by increased in cytosolic Rab5 and decreased colocalization of Rab5 with the endosomal
569 EEA1 (Figure 6A-C). These phenotypes correlated to a defect in endosomal sorting (Figure 1E) and a
570 block in transferrin uptake (Figure 6D,E), which may be yet another protective mechanism in order to
571 avoid iron overload and toxicity associated with neurodegeneration (Nunez, Urrutia et al., 2012).
572 Interestingly, hippocampal HT-22 neurons exposed to excess iron exhibit mitochondrial fragmentation
573 and a decrease in cell viability (Park, Lee et al., 2015). The metabolic effect of H₂O₂ on OCR is
574 intriguing. Mitochondria require oxygen to produce ATP to drive energy-consuming reactions (Batic
575 & Trifunovic, 2010). The observed decrease in OCR (Figure 5E) may serve to lower cellular
576 respiration and prevent further ROS production.

577 If the stress response triggers solubilization of Rab5 from EE, then it must also catalyze the
578 activation of Rab5 on mitochondria. We discovered that this step depends on Alsin. The C-terminal
579 VPS9 domain of Alsin has GEF activity towards Rab5, and plays a role in Rab5 endosomal
580 localization and dynamics (Otomo, Hadano et al., 2003, Topp, Gray et al., 2004). However, the

581 physiological role of Alsin with respect to Rab5 and endosomal activity has remained somewhat
582 mysterious. At steady state, Alsin is mainly cytosolic with a fraction localizing to vesicular-like
583 structures (Figure 10—figure supplement 1C) (Millecamps, Gentil et al., 2005). In stress-induced
584 conditions, however, Alsin re-localizes to mitochondria. The N-terminal RLD of Alsin has been shown
585 to exhibit an autoinhibitory effect on its VPS9 domain (Otomo et al., 2003). We posit that
586 mitochondrial-induced stress triggers structural changes in the protein, releasing the autoinhibitory
587 effect of RLD, thereby exposing the VSP9 domain for Rab5 activation and recruitment. Alsin was
588 required for Rab5 translocation to mitochondria as this was severely diminished in Alsin^{-/-} iPS-sMN
589 cells. The presence of (low levels) Rabex-5 on mitochondria (Figure 10A,C) detected in HeLa cells
590 suggests that other GEFs may contribute to some Rab5 activation, depending on the cell types, but
591 cannot fully compensate for the loss of Alsin function. A homologous gene, ALS2CL, containing only
592 the carboxyl-terminal half of ALS2, may also play a role by specifically binding to Rab5 and forming a
593 homodimer with the full-length Alsin to membranous compartments (Hadano, Otomo et al., 2004,
594 Suzuki-Utsunomiya, Hadano et al., 2007).

595 What is the function of the assembly of Rab5 and Rab5 machinery (Alsin and Rabenosyn-5) on
596 mitochondria besides its protective role? The stress response triggers remodeling of mitochondria to
597 confer molecular features characteristic of the endocytic system. The Rab5 machinery may be used to
598 bring mitochondria in close proximity to EE and form MCS (Figure 1). These MCS may mediate the
599 transfer of lipids and metabolites (Helle, Kanfer et al., 2013), or involve in “patching” up
600 mitochondrial wounds by recruiting the ESCRT machinery for closure, or other endomembranes for
601 fusion, both of which are observed in the PM-repair response (Jimenez, Maiuri et al., 2014, Reddy,
602 Caler et al., 2001). Worth noting from our EM study, we observed ER-like membranous structure in
603 contact with stressed mitochondria (Figure 3C) and considering the role of ER-mitochondria contacts

604 in Ca^{2+} -regulated apoptosis (Pinton, Giorgi et al., 2008), one may postulate that an orchestrated three-
605 way organelle crosstalk exists.

606 Considering that Rab5 is necessary for the biogenesis of the endolysosomal system (Zeigerer et
607 al., 2012), the Rab5 translocation may be a priming step of a stress response pathway that subjects
608 mitochondria to interact with the entire endolysosomal system, in order to modulate the mitochondrial
609 apoptotic potential. One quality control mechanism is the formation of mitochondrial-derived vesicles
610 (MDVs), which are involved in the transport of oxidized or damaged cargo to LE and lysosomes for
611 degradation (Soubannier, McLelland et al., 2012). This process depends on PINK1/Parkin (McLelland,
612 Soubannier et al., 2014), but can also occur independently (Matheoud, Sugiura et al., 2016). Rab5 may
613 play a role in MDV formation, although we could not detect vesicle budding events in our
614 experimental conditions. Once recruited onto mitochondria, Rab5 activity may not be limited to the
615 recruitment of its effectors, but initiate a more extensive endosomal Rab cascade via the Rab
616 coupling/conversion mechanism. On EE, Rab5 interacts with divalent effectors, coupling its activity to
617 other Rab proteins (e.g. Rab4, Rab11) that are required for receptor recycling (de Renzis, Sonnichsen
618 et al., 2002, Vitale, Rybin et al., 1998). Rab5 also initiates the activation of Rab7, resulting in the
619 conversion of EE into LE (Rink, Ghigo et al., 2005). The Rab coupling/conversion may also be
620 initiated on the mitochondria. Therefore, it is possible that the mitochondria-endosome MCS may
621 evolve over time leading to a Rab7-dependent mitophagic pathway (Jimenez-Orgaz, Kvainickas et al.,
622 2017), the engulfment of mitochondria by the EE (Hammerling, Najor et al., 2017), or conventional
623 autophagic processes (Ao, Zou et al., 2014, Stolz, Ernst et al., 2014). Future work exploring the
624 dynamics of other endosomal Rab GTPases in relation to Rab5 will be necessary to elucidate the
625 precise role of the endosomal system on mitochondria.

626 The physiological role of Alsin, although elusive, has been linked to both endosomes and
627 mitochondria. Cultured hippocampal neurons from Alsin knockout mice display an accumulation of
628 enlarged Rab5 endosomes and a reduced endosomal motility (Lai, Xie et al., 2009). Mutational and
629 linkage analysis of Alsin from human patients show that the VPS9 domain is critical for Alsin function
630 (Daud, Kakar et al., 2016, Verschuuren-Bemelmans, Winter et al., 2008). A recent EM study on the
631 corticospinal motor neurons (CSMN) from Alsin KO mice reveals a selective morphological defect in
632 mitochondria with enlarged core and broken cristae (Gautam, Jara et al., 2016). Interestingly, WT vs
633 Alsin KO CSMN show no change in Parkin expression, suggesting that mitophagy does not play a
634 major role (Gautam et al., 2016). We postulate that the pathological condition of mitochondrial defects
635 in Alsin KO cells is related to a deficiency in Rab5 recruitment to mitochondria, thereby leading to a
636 decline in protection from ROS and oxidative stress associated with aging. In ALS patients, motor
637 neurons likely accumulate more damaged mitochondria as age progresses, which eventually become an
638 overburden for cells.

639 The primary cause for ALS is still unclear, but oxidative stress is considered to be a major
640 contributor. Mutations in the anti-oxidant enzyme, superoxide dismutase 1 (SOD1), are associated with
641 motor neuron degeneration. In mouse models, an accumulation of the SOD1 mutant proteins results in
642 mitochondrial swelling and increased oxidative damage (Jaarsma, Rognoni et al., 2001). Interestingly,
643 loss of Alsin in the mutant SOD1 transgenic mice exacerbates and accelerates disease progression
644 (Hadano, Otomo et al., 2010). These studies, along with our findings, corroborate the protective role of
645 Alsin during oxidative stress. The mechanistic link between Rab5 and Alsin may present a general or
646 related mechanism in other neurodegenerative diseases. In Parkinson disease, the most common
647 mutation in the multidomain Leucine-rich repeat kinase 2 (LRRK2) protein leads to a hyper-activation
648 of the kinase domain, resulting in hyper-phosphorylation of a number of Rab GTPase substrates

649 including Rab5 (Steger, Diez et al., 2017, Steger, Tonelli et al., 2016). This may present yet another
650 mechanism of regulating Rab5 localization and function on mitochondria. Future work using different
651 neurodegenerative disease models in differentiated human neurons will provide deeper insights into the
652 disease etiology.

653

654 **Materials and Methods:**

655

656 **Cell lines, cell culture, and growth conditions**

657 The following cell lines have been validated and tested negative for mycoplasma contamination: HeLa
658 (Kyoto) cell line, BAC HeLa GFP expressing cell lines, and human KOLF_C1 iPSC (kindly provided
659 by Bill Skarnes, Sanger Institute). HeLa cells were cultured in high glucose DMEM (Gibco) with 10%
660 fetal bovine serum, 100 U/ml penicillin, 100 µg/ml streptomycin, and 2 mM glutamine (all reagents
661 from Sigma-Aldrich) with 5% CO₂ at 37°C. All plasmids were transfected using Effectene transfection
662 reagent (Qiagen) according to the manufacturer's protocol. All bacterial artificial chromosome (BAC)
663 transgene HeLa cell lines expressing different markers were obtained from the BAC recombineering
664 facility at MPI-CBG (Dresden, Germany) and generated using the method previously described (Poser,
665 Sarov et al., 2008).

666

667 **Plasmids and chemical reagents**

668 Construction of the pEGFP-C3-2xFYVE was made using mouse Hrs FYVE domain containing a
669 linker (QGQGS) (Raiborg, Bremnes et al., 2001). Human Rab5c cDNA was subcloned into the
670 pEGFP-C3 plasmid (Addgene). Human Alsin cDNA subcloned into the pEF1/Myc-His (Invitrogen)
671 plasmid was a kind gift from Dr. Ikuo Nishimoto (Kanekura, Hashimoto et al., 2004). Alexa-
672 conjugated transferrin (Invitrogen; T13342) and EGF (Invitrogen; E13345) were used at 25 µg/ml and
673 2 µg/ml, respectively. Carbonyl cyanide 3-chlorophenylhydrazone (CCCP) was purchased from Sigma
674 Aldrich (C2759). Stock solution was prepared to a final concentration of 10 mM in DMSO. 100 mM
675 Hydrogen peroxide (H₂O₂) (Merck Millipore; 7722-84-1) stock solution was prepared in PBS.

676

677 **Live-cell imaging**

678 Cells were seeded either in a 35-mm glass bottom dish or ibidi μ -Dish 35-mm, high Grid-500. Before
679 imaging, medium was replaced with HEPES-buffered DMEM without phenol red (Gibco). Time-lapse
680 imaging was performed using the Nikon TiE inverted stand microscope equipped with spinning disc
681 scan head (CSU-X1; Yokogawa), fast piezo objective z-positioner [Physik Instrumente], and back-
682 illuminated EMCCD camera (iXon EM+ DU-897 BV; Andor). Imaging was done with an Olympus
683 UPlanSApo 100x 1.4 Oil and Nikon Apo 100x 1.49 Oil DIC 0.13–0.20 objectives (illumination by
684 lasers: DPSS-488nm, DPSS-561nm, DPSS-640nm). Individual planes were recorded at ~11 frames per
685 sec with Z-stacks of three planes (step 0.3 μ m).

686

687 **Photosensitization of mitochondria**

688 Cells were incubated with MitoTracker Red CMXRos (ThermoFisher; M7512) at a final concentration
689 of 100 nM at 37°C for 30 min, 5% CO₂ incubator, and followed by 2X PBS wash before irradiating
690 with 561 nm laser on the spinning disc Andor-Olympus-IX71 at a low power dosage of ~5 J/cm² for 60
691 sec.

692

693 **Correlative light electron microscopy**

694 Cells were grown on a gridded dish (ibidi μ -Dish 35-mm, high Grid-500). Cells in different locations
695 were laser-treated with 561 nm laser for 30 sec. Cells were fixed in 2.5% glutaraldehyde/PBS for 30
696 min at room temperature. Post-fixation and embedding were performed using 1% osmium
697 tetroxide/1.5% potassium ferrocyanide and Epon Lx112, respectively. Sectioning of 150 nm thick UA
698 sections was performed on a Leica Ultracut UCT (Leica Microsystem, Wetzlar, Germany) with a

699 diamond knife. Samples were post-stained with 2% uranyl acetate and lead citrate. 2D images were
700 acquired on a Tecnai T12 (FEI, Hillsboro, Oregon, USA).

701

702 **Immunofluorescence and antibodies**

703 Cells were seeded on a ibidi Grid-500 glass bottom. After laser or H₂O₂ treatment, cells were fixed in
704 4% paraformaldehyde/PBS for 15 min at room temperature. Cells were washed twice with PBS and
705 permeabilized in PBS containing 0.1% saponin, and 1% BSA for 30 min at room temperature. Cells
706 were immunostained with the corresponding primary antibodies: anti-rabbit Rabenosyn-5/ZFYVE20
707 (Sigma Aldrich: HPA044878), anti-mouse EEA1 (BD Biosciences: 610457), anti-rabbit TOM20
708 (Santa Cruz Biotechnology: sc-11415), anti-rabbit APPL1 (Abcam: ab59592), anti-mouse APPL2
709 (home-made), anti-mouse Rab5 (BD Biosciences: 610724), anti-mouse cytochrome c (Abcam:
710 ab6311), and anti-rabbit Alsin (Novus Biological: NBP2-14284) antibodies. Alexa fluor-conjugated
711 (ThermoFisher) were used as secondary antibodies. Samples were mounted with Mowiol (Sigma-
712 Aldrich) on glass slides and examined using the Zeiss LSM 880 inverted single photon point scanning
713 confocal system with Quasar detector (32 spectral detection channels in the GaAsP detector plus
714 2PMTs) and transmitted light detector. Acquired images were processed and saved using the Zeiss
715 ZEN software. For immunofluorescence on iPSCs, smNPCs, and smNMs, cells were fixed with 4%
716 formaldehyde for 15 min, washed three times with wash buffer (0.3% Triton-X in PBS) for 5-10 min,
717 and blocked with blocking buffer (5% goat serum, 2% BSA, and 0.3% Triton-X in PBS) at room
718 temperature for 1 hr. Cells were incubated with primary antibodies in blocking buffer overnight at 4 °C.
719 After three washes with PBS for 10 min, cells were incubated with secondary antibodies in wash
720 buffer for 2-3 hr at room temperature followed by three washes in PBS for 10 min. Primary antibodies
721 used include: goat anti-ChAT (1:100) (Millipore, #AB144P), mouse anti-HB9 (1:50) (DSHB,

722 #81.5C10, conc.), rabbit anti-ISL1 (1:100) (Abcam, #ab20670), mouse anti-LIN28 (1:1000) (Cell
723 signaling, #5930S), chicken anti-MAP2 (1:1000) (Novus Biologicals, #NB300-213), mouse anti-
724 Nestin (1:150) (R&D Systems, #MAB1259), rabbit anti-OCT4 (1:500) (Abcam, #ab19857), rabbit
725 anti-PAX6 (1:300) (Covance, #PRB-278P), and rabbit anti-SOX2 (1:500) (Abcam, #ab97959). Ad-Ctrl
726 and Ad-tBid (a kind gift from Dr. Heidi McBride) were used at 1:200 PFU/cell.

727

728 **Transferrin uptake**

729 Cells were seeded in a 384-well plate and incubated with either complete medium or in the presence of
730 250 μ M H₂O₂ at 37°C for 2 hr. Cells were then pulsed with Alexa-647 Tfn (10 μ g/ml) for 5 min,
731 followed by 3x PBS wash, fixed with 3.7% PFA for 15 min, and then stained with DAPI (1:1000) and
732 CellMask Blue (1:2000) (ThermoFisher). Image acquisition was performed via the automated confocal
733 imaging system, CV7000S Yokogawa. Images analysis were performed using MotionTracking
734 software.

735

736 **Subcellular fractionation**

737 Cytosolic and mitochondrial fractions were performed using the mitochondria isolation kit, according
738 to the manufacturer's protocol with minor modification (ThermoFisher: cat89874). Cells ($\sim 1 \times 10^7$)
739 were resuspended in 400 μ l Mitochondrial Isolation Reagent A. Cells were chemically lysed by adding
740 5 μ l of Reagent B. After 5 min incubation on ice, 400 μ l of Reagent C was added to each sample and
741 centrifuged at 720 x g for 10 min. The post nuclear supernatant (PNS) was transferred to a new
742 eppendorf tube and centrifuged at 3000 x g for at 4°C for 15 min. For the total membrane and purified
743 cytosolic fractions, the PNS was clarified at 200,000g at 4°C for 1 hr. The resulting supernatant was
744 collected and trichloroacetic acid (TCA)/acetone precipitation was performed to obtain the final

745 cytosolic fraction. The remaining pellet was washed by adding 500 µl of Reagent C and centrifuged at
746 15,000 x g for 5 min. Final samples were resuspended in SDS loading buffer.

747

748 **Cytochrome c release assay and Western blot**

749 Cells were seeded on a 12-well plate. For hydrogen peroxide treatment, reagent was added directly into
750 the well to achieve the appropriate concentration. Separation of mitochondrial and cytosolic fractions
751 were performed using the mitochondrial isolation kit from ThermoFisher (cat:89874) with an
752 additional step of trichloroacetic acid precipitation of the cytosolic fraction. The final pellet was dried in
753 a 95°C heat block for 2-3 min before resuspending it in the SDS loading buffer. Cell lysates were
754 separated by SDS-PAGE, transferred onto the nitrocellulose membrane and blocked in 5% milk in
755 PBS containing 0.1% Tween. Primary and secondary antibodies were diluted in the blocking buffer and
756 incubated at room temperature for 2 hr. The bands were detected using the electrochemiluminescence
757 reagent and exposure onto x-ray films. The following antibodies were used in Western blot: anti-
758 mouse cytochrome c (Abcam: ab13575), anti-rabbit gamma tubulin (Sigma-Aldrich: T6557), anti-
759 rabbit Rabenosyn-5/ZFYVE20, anti-rabbit Alsin (Sigma Aldrich: SAB4200137), anti-mouse EEA1
760 (BD Biosciences: 610457), anti-rabbit APPL1 (Abcam: ab59592), anti-mouse APPL2 (home-made),
761 anti-mouse GAPDH (Sigma Aldrich: G8795), anti-mouse gamma tubulin (Sigma Aldrich: T6557), and
762 anti-rabbit TOM20 (Santa Cruz Biotechnology: sc-11415).

763

764 **The caspase-3/7 activation assay**

765 The caspase-3/7 activation in CCCP- vs H₂O₂- treated cells were measured using the caspase-3/7 green
766 flow cytometry assay kit (ThermoFisher: C10427). After 2 hr treatment, cells were scraped off per well
767 from a 6-well dish, gently resuspended in 1 ml of PBS containing 1 µl of green detection reagent, and

768 incubated at 37°C for 20 min. Samples were analyzed using the 488-nm excitation with standard
769 fluorescence compensation and emission filter (530/30 BP) in the FACS Calibur (Beckton Dickinson).
770 The gating was set based on the background signal in the DMSO control. The total cell count was set
771 to 5000. The caspase-3/7 activation in Alsin and Rab5 over-expressed cells was measured using the
772 caspase-3/7 green detection reagent (ThermoFisher: C10423). Cells were incubated in a complete
773 medium containing 5 µM of green detection reagent at 37°C for 30 min prior to fixation. Cells were
774 imaged using the Zeiss LSM 880 microscope.

775

776 **Measurements of mitochondrial oxygen consumption rates**

777 20,000 HeLa cells per well were seeded in a XFe96-well plate (Seahorse Bioscience), and grown to
778 ~80% confluency after overnight incubation. Cells were then equilibrated with a bicarbonate-free
779 DMEM medium containing 4 mM glutamine and 10 mM galactose in a 37°C ambient CO₂ incubator
780 for 1 hr, before starting the experiment. CCCP and H₂O₂ compounds were prepared fresh and diluted
781 in the assay medium, and were injected from the reagent ports at the indicated time. Oxygen
782 consumption rates (OCR) were measured using a Seahorse Extracellular Flux Analyzer.

783

784 **Generation of CRISPR/Cas9 knockout in human induced pluripotent cells**

785 Human KOLF_C1 iPSC were cultured in feeder-free conditions on Matrigel with TeSR-E8 media
786 (StemCell, Germany). For ALS2/Alsin knockout using CRISPR/Cas9 genome editing, 350,000 cells
787 were detached using Accutase, washed once with PBS and electroporated using the Neon Transfection
788 System (Invitrogen, Germany, 10ul kit, 1000V, 20ms, 3 pulses). The genomic sequence of human
789 Alsin was analyzed for CRISPR/Cas9 target sites by Geneious 8.1.6 software (Biomatters), and two
790 pairs of guides flanking a critical exon (exon3) were selected (5'-GCTAAAGTACTGAATTTTGG-3'

791 and 5'-AATAAAATCAGCAGGTGTGG-3'; 5'-GAATTTCTACAAAGTGCAGG-3' and 5'-
792 TAGCCTGGATGATGGCCGTT-3') and were used together to cause a frame shifting exon deletion.
793 The in vitro efficiency of these gRNAs was assessed by generating a genomic PCR cleavage template
794 of 3.4 bp (primers used: for-CCTCCCTTCCCAGGATCTGA and rev-
795 TGCTCAACTCGAGTGCCTTT; for-CAGGGTGAGCATCCCACATT and rev-
796 AGGAGTTCCAGTCAACCAGT) and incubating with recombinant Cas9. All gRNAs used in vitro
797 were identical in sequence to the DNA sense strand and not complementary to the mRNA sequence.
798 The RNAs employed in this method were chemically-modified and length optimized variants of the
799 native guide RNAs (Alt-R™ CRISPR crRNAs and tracrRNA, Integrated DNA Technologies,
800 Coralville, IA, USA). The recombinant Cas9 (provided by Protein Expression Facility at MPI-CBG)
801 protein from *Streptococcus pyogenes* was used. The crRNAs were mixed with trRNA and NLS-Cas9
802 (1 µg/µl). The guide RNA complex was formed by mixing the crRNAs and tracrRNAs in equal
803 amounts in Buffer R (Invitrogen, Germany) at 100 µM. Five days after electroporation, cells were
804 pooled and seeded for clonal dilution. Single clones were mechanically picked and amplified. Next,
805 genomic DNA was isolated using QuickExtract DNA Extraction Solution (EpiCentre, USA).
806 Homozygous deletions were verified by PCR and sequencing.

807

808 **Generation of iPSC-derived smNPC, and differentiation of smNPCs to sMNs**

809 All procedures were performed as previously described (Reinhardt, Glatza et al., 2013). Briefly, for
810 smNPC generation, iPSC colonies detached from Matrigel-coated wells (by 1 mg/ml dispase) were
811 resuspended in hESC medium (DMEM/F12, 20% KnockOUT Serum Replacement, 1%
812 Penicillin/Streptomycin/Glutamine, 0.1 mM Non-Essential Amino Acids Solution, 0.05 mM beta-
813 mercaptoethanol, without bFGF supplemented with 10 µM SB431542 (Tocris, #1614), 1 µM

814 dorsomorphin (Tocris, #3093), 3 μ M CHIR99021 (Axon Medchem, #Axon-1386) and 0.5 μ M
815 purmorphamine (STEMCELL Technologies, #72202), and cultured in non-coated petri dishes. After
816 two days, hESC medium was replaced by N2B27 medium (1:1 mixture of DMEM/F12 and Neurobasal
817 medium, 1% Penicillin/Streptomycin/Glutamine, 1:100 B-27 supplement minus vitamin A, 1:200 N-2
818 supplement) and supplemented with the same small molecules as listed above. After another two days,
819 culture medium was replaced by smNPC expansion medium (N2B27 medium supplemented with 150
820 μ M ascorbic acid (Sigma, #A4403), 3 μ M CHIR99021 and 0.5 μ M purmorphamine). On day 6 of
821 neural induction, embryonic bodies were broken into smaller clumps by titration and plated in 6 wells
822 of a Matrigel-coated 12-well plate. On day 9, cells were passaged for the first time using Accutase at a
823 1:3 split ratio and seeded in 4 wells of a Matrigel-coated 6-well plate. Afterwards, cells were passaged
824 once a week and seeded at a density of 1×10^6 cells per well. To obtain a highly pure smNPC culture,
825 smNPCs were propagated for at least 10 passages in smNPC expansion medium. For differentiation of
826 smNPC to MNs, smNPCs were seeded at a density of 1.5×10^6 cells per one well of a Matrigel-coated
827 6-well plate and cultured in N2B27 medium supplemented with 1 μ M purmorphamine for the first two
828 days of differentiation. The cells were then cultured in N2B27 medium supplemented with 1 μ M
829 purmorphamine and 1 μ M retinoic acid (Sigma, #R2625) until day 9 of differentiation. On day 9, cells
830 were dissociated using Accutase and plated on polyornithine/laminin-coated ibidi μ -slides (at a density
831 of 150000 cells per well) or Nunc 4-well plates (at a density of 300.000 cells per well) in maturation
832 medium (N2B27 medium supplemented with 0.5 mM cAMP (Sigma, #D0627), 10 ng/ml BDNF
833 (Peprotech, #450-02-10), and 10 ng/ml GDNF (Peprotech, #450-10-10)). Cells were maintained in
834 maturation medium until analysis on day 28.

835

836 **Image and statistical analysis**

837 Image resizing, cropping and brightness were uniformly adjusted in Fiji (<http://fiji.sc/>). Colocalization

838 analysis was performed using MotionTracking software (Rink et al., 2005) (<http://motiontracking.mpi->
839 [cbg.de/get/](http://motiontracking.mpi-cbg.de/get/)) and described previously (Gilleron, Querbes et al., 2013). The y-axis is expressed as the
840 ratio of co-localized objects (eg. A to B) to total objects found in A. Final images were assembled
841 using Adobe Photoshop and Illustrator. Densitometry quantification were performed in Fiji following
842 the previously described protocol (<http://www.yorku.ca/yisheng/Internal/Protocols/ImageJ.pdf>). P-
843 values were calculated by two-tailed t-test using GraphPad Prism7.

844

845 **Acknowledgements**

846 We thank the MPI-CBG light microscopy facility for access and technical assistance; the
847 TransgeneOmics facility and Hyman lab, especially Mihail Sarov, Aleksandra Syta, Kathleen Rönsch,
848 Marit Leuschner, and Ina Poser, for the design, generation, and maintenance of the CRISPR/Cas9 KO
849 iPSC lines; Julia Japtok from the lab of Andreas Hermann for sharing protocols for the smNPC
850 generation and MN differentiation; Weihua Leng and Urska Repnik for technical assistance and
851 method discussion for electron microscopy; Ina Nuesslein and Christina Eugster from the MPI-CBG
852 FACS facility for assistance on the flow cytometry; Rico Barsacchi from the Technology Development
853 Studio facility for assistance with the transferrin uptake and Seahorse Analyzer; Yannis Kalaidzidis for
854 assistance with MotionTracking software; and Heidi McBride for reagents, discussion and feedback.

855

856 **Competing interests**

857 No competing interests exist.

858

859 **References:**

- 860 Ao X, Zou L, Wu Y (2014) Regulation of autophagy by the Rab GTPase network. *Cell death and*
861 *differentiation* 21: 348-58
- 862 Bratic I, Trifunovic A (2010) Mitochondrial energy metabolism and ageing. *Biochimica et biophysica*
863 *acta* 1797: 961-7
- 864 Cavalli V, Vilbois F, Corti M, Marcote MJ, Tamura K, Karin M, Arkininstall S, Gruenberg J (2001) The
865 stress-induced MAP kinase p38 regulates endocytic trafficking via the GDI:Rab5 complex. *Mol Cell* 7:
866 421-32
- 867 Cosulich SC, Horiuchi H, Zerial M, Clarke PR, Woodman PG (1997) Cleavage of rabaptin-5 blocks
868 endosome fusion during apoptosis. *The EMBO journal* 16: 6182-91
- 869 Daud S, Kakar N, Goebel I, Hashmi AS, Yaqub T, Nurnberg G, Nurnberg P, Morris-Rosendahl DJ,
870 Wasim M, Volk AE, Kubisch C, Ahmad J, Borck G (2016) Identification of two novel ALS2
871 mutations in infantile-onset ascending hereditary spastic paraplegia. *Amyotrophic lateral sclerosis &*
872 *frontotemporal degeneration* 17: 260-5
- 873 de Hoop MJ, Huber LA, Stenmark H, Williamson E, Zerial M, Parton RG, Dotti CG (1994) The
874 involvement of the small GTP-binding protein Rab5a in neuronal endocytosis. *Neuron* 13: 11-22
- 875 de Renzis S, Sonnichsen B, Zerial M (2002) Divalent Rab effectors regulate the sub-compartmental
876 organization and sorting of early endosomes. *Nature cell biology* 4: 124-33
- 877 Del Conte-Zerial P, Bruschi L, Rink JC, Collinet C, Kalaidzidis Y, Zerial M, Deutsch A (2008)
878 Membrane identity and GTPase cascades regulated by toggle and cut-out switches. *Mol Syst Biol* 4:
879 206
- 880 Galloway CA, Yoon Y (2013) Mitochondrial morphology in metabolic diseases. *Antioxidants & redox*
881 *signaling* 19: 415-30
- 882 Gautam M, Jara JH, Sekerkova G, Yasvoina MV, Martina M, Ozdinler PH (2016) Absence of alsin
883 function leads to corticospinal motor neuron vulnerability via novel disease mechanisms. *Human*
884 *molecular genetics* 25: 1074-87
- 885 Gilleron J, Querbes W, Zeigerer A, Borodovsky A, Marsico G, Schubert U, Manygoats K, Seifert S,
886 Andree C, Stoter M, Epstein-Barash H, Zhang L, Koteliansky V, Fitzgerald K, Fava E, Bickle M,
887 Kalaidzidis Y, Akinc A, Maier M, Zerial M (2013) Image-based analysis of lipid nanoparticle-
888 mediated siRNA delivery, intracellular trafficking and endosomal escape. *Nature biotechnology* 31:
889 638-46
- 890 Hadano S, Otomo A, Kunita R, Suzuki-Utsunomiya K, Akatsuka A, Koike M, Aoki M, Uchiyama Y,
891 Itoyama Y, Ikeda JE (2010) Loss of ALS2/Alsin exacerbates motor dysfunction in a SOD1-expressing
892 mouse ALS model by disturbing endolysosomal trafficking. *PloS one* 5: e9805
- 893 Hadano S, Otomo A, Suzuki-Utsunomiya K, Kunita R, Yanagisawa Y, Showguchi-Miyata J,
894 Mizumura H, Ikeda JE (2004) ALS2CL, the novel protein highly homologous to the carboxy-terminal
895 half of ALS2, binds to Rab5 and modulates endosome dynamics. *FEBS letters* 575: 64-70
- 896 Hammerling BC, Najor RH, Cortez MQ, Shires SE, Leon LJ, Gonzalez ER, Boassa D, Phan S, Thor A,
897 Jimenez RE, Li H, Kitsis RN, Dorn II GW, Sadoshima J, Ellisman MH, Gustafsson AB (2017) A Rab5
898 endosomal pathway mediates Parkin-dependent mitochondrial clearance. *Nat Commun* 8: 14050
- 899 Helle SC, Kanfer G, Kolar K, Lang A, Michel AH, Kornmann B (2013) Organization and function of
900 membrane contact sites. *Biochimica et biophysica acta* 1833: 2526-41
- 901 Jaarsma D, Rognoni F, van Duijn W, Verspaget HW, Haasdijk ED, Holstege JC (2001) CuZn
902 superoxide dismutase (SOD1) accumulates in vacuolated mitochondria in transgenic mice expressing
903 amyotrophic lateral sclerosis-linked SOD1 mutations. *Acta neuropathologica* 102: 293-305

904 Jimenez AJ, Maiuri P, Lafaurie-Janvore J, Divoux S, Piel M, Perez F (2014) ESCRT machinery is
905 required for plasma membrane repair. *Science* 343: 1247136

906 Jimenez-Orgaz A, Kvainickas A, Nagele H, Denner J, Eimer S, Dengjel J, Steinberg F (2017) Control
907 of RAB7 activity and localization through the retromer-TBC1D5 complex enables RAB7-dependent
908 mitophagy. *The EMBO journal*

909 Kalaidzidis I, Miaczynska M, Brewinska-Olchowik M, Hupalowska A, Ferguson C, Parton RG,
910 Kalaidzidis Y, Zerial M (2015) APPL endosomes are not obligatory endocytic intermediates but act as
911 stable cargo-sorting compartments. *The Journal of cell biology* 211: 123-44

912 Kanekura K, Hashimoto Y, Niikura T, Aiso S, Matsuoka M, Nishimoto I (2004) Alsin, the product of
913 ALS2 gene, suppresses SOD1 mutant neurotoxicity through RhoGEF domain by interacting with
914 SOD1 mutants. *The Journal of biological chemistry* 279: 19247-56

915 Lai C, Xie C, Shim H, Chandran J, Howell BW, Cai H (2009) Regulation of endosomal motility and
916 degradation by amyotrophic lateral sclerosis 2/alsin. *Molecular brain* 2: 23

917 Lippe R, Miaczynska M, Rybin V, Runge A, Zerial M (2001) Functional synergy between Rab5
918 effector Rabaptin-5 and exchange factor Rabex-5 when physically associated in a complex. *Molecular
919 biology of the cell* 12: 2219-28

920 Mace G, Miaczynska M, Zerial M, Nebreda AR (2005) Phosphorylation of EEA1 by p38 MAP kinase
921 regulates mu opioid receptor endocytosis. *The EMBO journal* 24: 3235-46

922 Matheoud D, Sugiura A, Bellemare-Pelletier A, Laplante A, Rondeau C, Chemali M, Fazel A,
923 Bergeron JJ, Trudeau LE, Burelle Y, Gagnon E, McBride HM, Desjardins M (2016) Parkinson's
924 Disease-Related Proteins PINK1 and Parkin Repress Mitochondrial Antigen Presentation. *Cell* 166:
925 314-327

926 McLelland GL, Soubannier V, Chen CX, McBride HM, Fon EA (2014) Parkin and PINK1 function in
927 a vesicular trafficking pathway regulating mitochondrial quality control. *The EMBO journal* 33: 282-
928 95

929 Millegamps S, Gentil BJ, Gros-Louis F, Rouleau G, Julien JP (2005) Alsin is partially associated with
930 centrosome in human cells. *Biochimica et biophysica acta* 1745: 84-100

931 Murray DH, Jahnel M, Lauer J, Avellaneda MJ, Brouilly N, Cezanne A, Morales-Navarrete H, Perini
932 ED, Ferguson C, Lupas AN, Kalaidzidis Y, Parton RG, Grill SW, Zerial M (2016) An endosomal
933 tether undergoes an entropic collapse to bring vesicles together. *Nature* 537: 107-111

934 Nunez MT, Urrutia P, Mena N, Aguirre P, Tapia V, Salazar J (2012) Iron toxicity in
935 neurodegeneration. *Biometals* 25: 761-76

936 Ohya T, Miaczynska M, Coskun U, Lommer B, Runge A, Drechsel D, Kalaidzidis Y, Zerial M (2009)
937 Reconstitution of Rab- and SNARE-dependent membrane fusion by synthetic endosomes. *Nature* 459:
938 1091-7

939 Otomo A, Hadano S, Okada T, Mizumura H, Kunita R, Nishijima H, Showguchi-Miyata J,
940 Yanagisawa Y, Kohiki E, Suga E, Yasuda M, Osuga H, Nishimoto T, Narumiya S, Ikeda JE (2003)
941 ALS2, a novel guanine nucleotide exchange factor for the small GTPase Rab5, is implicated in
942 endosomal dynamics. *Human molecular genetics* 12: 1671-87

943 Park J, Lee DG, Kim B, Park SJ, Kim JH, Lee SR, Chang KT, Lee HS, Lee DS (2015) Iron overload
944 triggers mitochondrial fragmentation via calcineurin-sensitive signals in HT-22 hippocampal neuron
945 cells. *Toxicology* 337: 39-46

946 Pinton P, Giorgi C, Siviero R, Zecchini E, Rizzuto R (2008) Calcium and apoptosis: ER-mitochondria
947 Ca²⁺ transfer in the control of apoptosis. *Oncogene* 27: 6407-18

948 Poser I, Sarov M, Hutchins JR, Heriche JK, Toyoda Y, Pozniakovsky A, Weigl D, Nitsche A,
949 Hegemann B, Bird AW, Pelletier L, Kittler R, Hua S, Naumann R, Augsburg M, Sykora MM,

950 Hofemeister H, Zhang Y, Nasmyth K, White KP et al. (2008) BAC TransgeneOmics: a high-
951 throughput method for exploration of protein function in mammals. *Nature methods* 5: 409-15
952 Raiborg C, Bremnes B, Mehлум A, Gillooly DJ, D'Arrigo A, Stang E, Stenmark H (2001) FYVE and
953 coiled-coil domains determine the specific localisation of Hrs to early endosomes. *Journal of cell*
954 *science* 114: 2255-63
955 Reddy A, Caler EV, Andrews NW (2001) Plasma membrane repair is mediated by Ca(2+)-regulated
956 exocytosis of lysosomes. *Cell* 106: 157-69
957 Reinhardt P, Glatza M, Hemmer K, Tsytsyura Y, Thiel CS, Hoing S, Moritz S, Parga JA, Wagner L,
958 Bruder JM, Wu G, Schmid B, Ropke A, Klingauf J, Schwamborn JC, Gasser T, Scholer HR,
959 Sternecker J (2013) Derivation and expansion using only small molecules of human neural
960 progenitors for neurodegenerative disease modeling. *PloS one* 8: e59252
961 Rink J, Ghigo E, Kalaidzidis Y, Zerial M (2005) Rab conversion as a mechanism of progression from
962 early to late endosomes. *Cell* 122: 735-49
963 Sena LA, Chandel NS (2012) Physiological roles of mitochondrial reactive oxygen species. *Mol Cell*
964 48: 158-67
965 Soubannier V, McLelland GL, Zunino R, Braschi E, Rippstein P, Fon EA, McBride HM (2012) A
966 vesicular transport pathway shuttles cargo from mitochondria to lysosomes. *Current biology : CB* 22:
967 135-41
968 Steger M, Diez F, Dhekne HS, Lis P, Nirujogi RS, Karayel O, Tonelli F, Martinez TN, Lorentzen E,
969 Pfeffer SR, Alessi DR, Mann M (2017) Systematic proteomic analysis of LRRK2-mediated Rab
970 GTPase phosphorylation establishes a connection to ciliogenesis. *eLife* 6
971 Steger M, Tonelli F, Ito G, Davies P, Trost M, Vetter M, Wachter S, Lorentzen E, Duddy G, Wilson S,
972 Baptista MAS, Fiske BK, Fell MJ, Morrow JA, Reith AD, Alessi DR, Mann M (2016)
973 Phosphoproteomics reveals that Parkinson's disease kinase LRRK2 regulates a subset of Rab GTPases.
974 *eLife* 5
975 Stolz A, Ernst A, Dikic I (2014) Cargo recognition and trafficking in selective autophagy. *Nature cell*
976 *biology* 16: 495-501
977 Sun G, Guzman E, Balasanyan V, Conner CM, Wong K, Zhou HR, Kosik KS, Montell DJ (2017) A
978 molecular signature for anastasis, recovery from the brink of apoptotic cell death. *The Journal of cell*
979 *biology* 216: 3355-3368
980 Suzuki-Utsunomiya K, Hadano S, Otomo A, Kunita R, Mizumura H, Osuga H, Ikeda JE (2007)
981 ALS2CL, a novel ALS2-interactor, modulates ALS2-mediated endosome dynamics. *Biochem Biophys*
982 *Res Commun* 354: 491-7
983 Swanton E, Bishop N, Woodman P (1999) Human rabaptin-5 is selectively cleaved by caspase-3
984 during apoptosis. *The Journal of biological chemistry* 274: 37583-90
985 Tang HL, Tang HM, Mak KH, Hu S, Wang SS, Wong KM, Wong CS, Wu HY, Law HT, Liu K,
986 Talbot CC, Jr., Lau WK, Montell DJ, Fung MC (2012) Cell survival, DNA damage, and oncogenic
987 transformation after a transient and reversible apoptotic response. *Molecular biology of the cell* 23:
988 2240-52
989 Topp JD, Gray NW, Gerard RD, Horazdovsky BF (2004) Alsln is a Rab5 and Rac1 guanine nucleotide
990 exchange factor. *The Journal of biological chemistry* 279: 24612-23
991 Verschuuren-Bemelmans CC, Winter P, Sival DA, Elting JW, Brouwer OF, Muller U (2008) Novel
992 homozygous ALS2 nonsense mutation (p.Gln715X) in sibs with infantile-onset ascending spastic
993 paralysis: the first cases from northwestern Europe. *European journal of human genetics : EJHG* 16:
994 1407-11

995 Vitale G, Rybin V, Christoforidis S, Thornqvist P, McCaffrey M, Stenmark H, Zerial M (1998)
996 Distinct Rab-binding domains mediate the interaction of Rabaptin-5 with GTP-bound Rab4 and Rab5.
997 The EMBO journal 17: 1941-51
998 Zeigerer A, Gilleron J, Bogorad RL, Marsico G, Nonaka H, Seifert S, Epstein-Barash H, Kuchimanchi
999 S, Peng CG, Ruda VM, Del Conte-Zerial P, Hengstler JG, Kalaidzidis Y, Koteliansky V, Zerial M
1000 (2012) Rab5 is necessary for the biogenesis of the endolysosomal system in vivo. Nature 485: 465-70
1001 Zerial M, McBride H (2001) Rab proteins as membrane organizers. Nature reviews Molecular cell
1002 biology 2: 107-17
1003 Zhang Z, Zhang T, Wang S, Gong Z, Tang C, Chen J, Ding J (2014) Molecular mechanism for Rabex-
1004 5 GEF activation by Rabaptin-5. eLife 3
1005

1006

1007 **Figure Legends:**

1008

1009 **Figure 1. Endosomal contacts with mitochondria.** (A) and (B) HeLa cells were transfected with
1010 TagRFP-MTS (mitochondria targeting sequence) and labeled with either Alexa-488 transferrin (Tfn)
1011 or epidermal growth factor (EGF) at 37°C for 10 min, respectively. (C) HeLa cells stained with Mito-
1012 Red were labeled with Tfn-488 or EGF-488 at 37°C for 10, 60 min, or treated with 250 μ M H₂O₂ after
1013 10 min labeling followed by additional 50 min incubation. Inset regions are shown. Scale bars, 10 μ m.
1014 (D) Colocalization analysis based on subtraction of random colocalization was performed between
1015 Mito-Red and Tfn-488 or EGF-488 from images obtained in Figure 1C, $n = 50$. (E) Quantification of
1016 total intensity per cell, $n = 50$. Error bars represent SEMs. P-values based on two-tailed t-tests.

1017

1018 **Figure 2. Recruitment of Rab5 to mitochondria upon laser-induced stress.** (A) Live BAC GFP-
1019 Rab5 HeLa cells were labeled with 100 nM Mito-Red at 37°C for 30 min. Cells were photoirradiated
1020 with a low dosage of 561 nm laser (~ 5 J/cm²) for 60 sec. A snapshot of a cell before (Pre) and 20 min
1021 post-laser were taken. Arrowheads indicate GFP-Rab5-positive endosomes that are in close proximity
1022 to mitochondria. (B) Colocalization analysis between Mito-Red and GFP-Rab5 after photoirradiation
1023 as performed in (A), $n = 5$. Error bars represent SEMs. P-values based on two-tailed t-tests. (C) Live-
1024 cell imaging of a BAC GFP-Rab5 HeLa cell treated the same way as in (A). (D) Quantification of the
1025 GFP fluorescent signal over a period of 30 min from the inset region in (C). (E) Time-lapsed images of
1026 Mito-Red, GFP-Rab5, and merged from the inset region in (C). (F) Live-cell imaging of a BAC GFP-
1027 Rab5 HeLa cell photoirradiated only to the marked region (white box). The cell before laser irradiation
1028 is shown (Pre). Snapshots of the cell were taken at 10 min and 20 min post-laser. Inset images show
1029 the effect of laser treatment on mitochondrial morphology and network. Arrowheads indicate the

1030 recruitment of GFP-Rab5 (filled) and GFP-Rab5-positive endosomes near mitochondria (double-head).
1031 Scale bars, 10 μm .

1032

1033 **Figure 2–figure supplement 1. Rab5 recruitment to mitochondria is specific to Mito-Red. (A)**

1034 HeLa cells were labeled with 100 nM MitoTracker-Green FM (Mito-Green) at 37°C for 30 min and
1035 photoirradiated with 561 nm laser ($\sim 10 \text{ J/cm}^2$) for 60 sec. Image was taken at 20 min post-laser

1036 treatment. Mitochondrial network remained tubular. **(B)** HeLa BAC GFP-Rab5 cells were transfected
1037 with TagRFP-MTS and photoirradiated with 561 nm laser ($\sim 10 \text{ J/cm}^2$) for 60 sec. Image was taken at

1038 20 min post-laser treatment. **(C)** BAC GFP-Rab5 cells were seeded on gridded glass dishes, labeled
1039 with Mito-Red for 30 min, photoirradiated as before, and fixed after 30 min post-laser. Cells were

1040 immunostained with specific antibodies against Rab5 or TOM20. Inset regions are shown. Scale bars,
1041 10 μm .

1042

1043 **Figure 2–figure supplement 2. GFP-Rab5 enrichment on mitochondria persist for <60 min.**

1044 Time-lapse images of a cell following laser treatment as in Figure 2F. Inset images are shown at
1045 different time points (min). Arrowheads indicate the recruitment of GFP-Rab5 to mitochondria within

1046 15 min, which sustain for at least 60 min. Scale bars, 10 μm .

1047

1048 **Figure 3. Membrane contacts between Rab5-positive mitochondria and endosomes.**

1049 Ultrastructural analysis of cells upon laser-induced stress. **(A)** Flow chart of the experimental set up.

1050 BAC GFP-Rab5 cells were seeded on gridded dishes, labeled with 100 nM Mito-Red at 37°C for 30
1051 min. A cell of interest was then photoirradiated with a low dosage of 561 nm laser ($\sim 5 \text{ J/cm}^2$) for 60

1052 sec. Live-cell imaging between GFP-Rab5-positive endosomes and mitochondria was assessed for

1053 organelle dynamics. The same cell was re-imaged for post-fixation analysis before processing for EM.
1054 **(B)** Fluorescent images of GFP-Rab5 and (Mito-Red) after fixation with glutaraldehyde. Box region
1055 shows a GFP-Rab5 endosome (red arrowhead) next to a swollen Rab5-positive mitochondrion. The
1056 transmission electron micrograph (TEM) of the same cell is shown (right panel). The nuclear
1057 membrane (dotted line) and mitochondria (red star) were used as fiducial markers. **(C)** Zoom-in
1058 images of the box region in **(B)**. Colored images indicate the GFP-Rab5-positive structure in green and
1059 mitochondrion in red. Raw images are shown below. Mitochondrial cristae are visible. The
1060 membranous structure adjacent to the mitochondrion likely corresponds to ER. Scale bars, 500 nm.

1061

1062 **Figure 4. Localization of endogenous LC3, Lamp1, Parkin, and Bax upon laser-induced stress.**

1063 BAC GFP-Rab5 cells were labeled with 100 nM Mito-Red at 37°C for 30 min. Cells were acquired
1064 prior to laser irradiation as controls (**A**), **(C)**, **(E)**, and **(G)**. Same cells were photoirradiated
1065 as before, fixed after 60 min post-laser treatment, and immunostained with specific antibodies against
1066 LC3 **(B)**, Lamp1 **(D)**, Parkin **(F)**, and Bax **(H)**. Inset images show the area before and after laser
1067 treatment. **(I)** Colocalization analysis of Mito-Red to Rab5, LC3, Lamp1, Parkin, and Bax, in untreated
1068 vs laser-induced conditions ($n = 3$). Untreated cells correspond to cells outside of the laser treated area.
1069 Error bars represent SEMs. P-values based on two-tailed t-tests. Scale bars, 10 μm .

1070

1071 **Figure 4–figure supplement 1. Localization of endogenous LC3, Lamp1, and Parkin in untreated**
1072 **cells.** BAC GFP-Rab5 cells were seeded on gridded glass dishes, and labeled with 100 nM Mito-Red at
1073 37°C for 30 min. Cells were fixed and immunostained with antibodies against LC3, Lamp1, and Parkin.
1074 Images were taken from the area outside of laser-treated cells. Scale bars, 10 μm .

1075

1076 **Figure 4–figure supplement 2. BAC GFP -LC3, -Lamp1, and -Parkin localization upon laser-**
1077 **induced stress.** Live-cell imaging of BAC GFP-LC3 (A), GFP-LAMP1 (B), and GFP-Parkin (C) cells.
1078 Cells were labeled with 100 nM Mito-Red at 37°C for 30 min and photoirradiated as before. Images of
1079 the same cell before (untreated) and 60 min post-laser treatment are shown. Inset images indicate the
1080 approximate area before and after laser treatment.

1081

1082 **Figure 4–figure supplement 3. CCCP induces Bax protein expression and localization on**
1083 **mitochondria.** (A) HeLa cells labeled with 100 nM Mito-Red were treated with either DMSO (Ctrl) or
1084 10 μ M CCCP at 37°C for 2 hr. Cells were fixed and immunostained with antibody against Bax. Scale
1085 bars, 10 μ m. (B) Fluorescence fold change of Bax signals between Ctrl and CCCP-treated cells; $n = 50$.
1086 Values in controls cells are normalized to one. (C) Colocalization analysis between Mito-Red and Bax
1087 in Ctrl vs CCCP. Error bars represent SEMs. P-values based on two-tailed t-tests.

1088

1089 **Figure 4–figure supplement 4. tBid over-expression leads to Rab5 enrichment on mitochondria.**
1090 BAC GFP-Rab5 cells were infected with control adenovirus (Ad-Ctrl) or Ad-tBid at 37°C for 12 hr.
1091 Cells were fixed and immunostained with TOM20 antibody. Inset regions are shown. Scale bars,
1092 10 μ m.

1093

1094 **Figure 5. Effects of CCCP vs H₂O₂ on Rab5 recruitment to mitochondria.** BAC GFP-Rab5 HeLa
1095 cells labeled with 100 nM of Mito-Red were treated with either DMSO (Ctrl), 10 μ M CCCP (A), or
1096 250 μ M H₂O₂ at 37°C for 2 hr (B). Cells were fixed and imaged by confocal microscopy. Inset regions
1097 reveal the effect on mitochondrial morphology and GFP-Rab5 localization upon treatment.
1098 Arrowheads indicate rounded and stressed mitochondria in both CCCP- and H₂O₂- treated conditions.

1099 Scale bars, 10 μm . (C) and (D) Colocalization analysis between Mito-Red and GFP-Rab5 in (A) and
1100 (B), respectively; $n = 50$. Error bars represent SEMs. P-values based on two-tailed t-tests. (E)
1101 Subcellular fractionation was performed in HeLa cells treated with DMSO (Ctrl), 10 μM CCCP, or 250
1102 μM H_2O_2 at 37°C for 2 hr. Protein samples from purified mitochondria (Mito) and cytosolic (C)
1103 fractions were loaded onto SDS-PAGE and immunoblotted with cytochrome c antibody. (F) Cells were
1104 treated the same way as in (E). Cells were then resuspended in live-cell imaging solution containing
1105 500 nM caspase-3/7 green flow cytometric reagent and incubated at 37°C for 30 min before subjecting
1106 to flow cytometric analysis. FITC signal (x-axis) is plotted against the total cell count (y-axis). The
1107 gating was set based on the background signal in DMSO control. (G) HeLa cells were seeded in the
1108 Seahorse 96-well plate format and incubated overnight. Growth medium was exchanged to
1109 bicarbonated-free low-buffered assay medium (provided by the manufacturer) supplemented with 10
1110 mM galactose immediately before the start of the experiment. Oxygen consumption rate measurements
1111 were measured in the Seahorse XFe96 Analyzer from cells injected with media only (purple), 250 μM
1112 H_2O_2 (green), or 10 μM CCCP (orange). Error bars represent SEMs.

1113

1114 **Figure 5–figure supplement 2. CCCP, but not H_2O_2 , leads to Parkin recruitment.** (A) BAC GFP-
1115 Parkin or WT HeLa cells (B) were treated with either DMSO (Ctrl), 10 μM CCCP, or 250 μM H_2O_2 at
1116 37°C for 2 hr. Cells were fixed and imaged by confocal microscopy. HeLa cells were immunostained
1117 with Parkin antibody. Inset regions are shown. Scale bars, 10 μm .

1118

1119 **Figure 6. Hydrogen peroxide (H_2O_2) treatment decreases Rab5 membrane association on EE,**
1120 **increases early endosomal-mitochondrial contacts, and reduces transferrin uptake.** (A)

1121 Subcellular fractionation was performed in HeLa cells treated with H_2O_2 for 1 and 2 hr. The total

1122 membrane (M) fraction was obtained by centrifugation of the post nuclear supernatant at 200,000 g at
1123 4°C for 1 hr, and supernatant was taken as cytosolic (C) fraction. Protein samples were loaded onto
1124 SDS-PAGE and immunoblotted with antibodies against Rab5, EEA1, GAPDH, and TOM20. The long
1125 exposure blot for EEA1 is shown (right panel). **(B)** Densitometric quantification of Rab5 in **(A)**. Band
1126 intensities were calculated as normalized ratio between Rab5 to TOM20 in the M fraction, and Rab5 to
1127 GAPDH in the C fraction. Fold change is plotted on the y-axis. Error bars represent SEMs from 3
1128 independent experiments. **(C)** BAC GFP-Rab5 HeLa cells were incubated with/out 250 μM H_2O_2 at
1129 37°C for 2 hr. Cells were fixed and immunostained with EEA1 antibody. Colocalization analysis was
1130 performed between GFP-Rab5 and EEA1. **(D)** HeLa cells were seeded in a 384-well plate and pre-
1131 treated with either PBS (control) or 250 μM H_2O_2 at 37°C for 10 min. Cells were then pulsed with
1132 Alexa-647 Tfn (10 $\mu\text{g}/\text{ml}$) for 5 min, washed with PBS, fixed, and stained with DAPI (nuclear) and
1133 CellMask Blue (cytoplasmic) dyes. Images were acquired by the Yagokawa confocal microscope.
1134 Scale bars, 10 μm . **(E)** Quantification of the cytoplasmic fluorescence intensity per cell, $n = 50$. P-
1135 values based on two-tailed t-tests.

1136

1137 **Figure 7. Rab5 regulates cytochrome c release during H_2O_2 -induced stress.** **(A)** Live-cell imaging
1138 of a BAC GFP-Rab5 cell stained with 100 nM Mito-Red before (0 min) and after treatment (60 min)
1139 with 250 μM H_2O_2 at 37°C. Inset images are shown and arrowheads indicate GFP-Rab5 recruitment to
1140 MOMP events (right panel). Scale bars, 10 μm . **(B)** HeLa cells over-expressing either GFP or GFP-
1141 Rab5 were treated with 250 μM H_2O_2 at 37°C for 1 to 4 hr. Protein samples from cytosolic fractions
1142 were obtained and immunoblotted for cytochrome c and tubulin (as a loading control). **(C)**
1143 Densitometric quantification of cytochrome c release in **(B)**. Data were collected from three

1144 independent experiments. Y-axis corresponds to the normalized ratio intensity of cytochrome c to the
1145 tubulin loading control. P-values based on two-tailed t-tests.

1146

1147 **Figure 8. H₂O₂-induced translocation of Rab5 to mitochondria is reversible.** HeLa cells were
1148 seeded in 24-well plates (**A**) or on glass coverslips (**B**), and after overnight incubation, were treated
1149 with either 250 μ M or 500 μ M H₂O₂ at 37°C for 0, 6, 12, 24 hr, or replaced with a fresh medium at 12
1150 hr followed by additional 12 hr incubation. (**A**) Cells were then harvested in SDS loading buffer and
1151 protein lysates were loaded onto SDS-PAGE and immunoblotted with TOM20 and GAPDH antibodies.
1152 (**B**) Cells were fixed and immunostained with Rab5 and TOM20 antibodies. Inset regions are shown.
1153 Scale bars, 10 μ m. (**C**) Colocalization analysis between TOM20 and Rab5 in (**B**), $n = 50$. P-values
1154 based on two-tailed t-tests.

1155

1156 **Figure 9. Localization of Rab5 effectors upon mitochondrial stress.** BAC GFP-Rab5 cells seeded
1157 on gridded dishes were labeled with Mito-Red and photoirradiated as before. Cells were fixed after 30
1158 min post-laser treatment and immunostained with antibodies against ZFYVE20 and EEA1 (**A**), or
1159 APPL1 and APPL2 (**B**). Inset regions are shown. Scale bars, 10 μ m. (**C**) Colocalization analysis from
1160 untreated and laser-treated cells in (**A**) and (**B**), $n = 3$. P-values based on two-tailed t-tests. (**D**)
1161 Subcellular fractionation was performed in HeLa cells treated with either PBS (control) or 250 μ M
1162 H₂O₂ at 37°C for 2 hr. Protein samples from purified mitochondria (Mito) and cytosolic (C) fractions
1163 were loaded onto SDS-PAGE and immunoblotted with antibodies against Rab5, EEA1, Rabenosyn-5,
1164 APPL1, APPL2, and TOM20.

1165

1166 **Figure 9–figure supplement 1. Localization of endogenous Rabenosyn-5, EEA1, APPL1 and**
1167 **APPL2.** BAC GFP-Rab5 cells were seeded on glass coverslips, fixed, and immunostained with
1168 antibodies against Rabenosyn-5 (**A**), EEA1 (**B**), APPL1 (**C**), and APPL2 (**D**). Inset regions are shown.
1169 Scale bars, 10 μ m.

1170

1171 **Figure 9–figure supplement 2. Localization of GFP-2xFYVE^{Hrs} upon laser-induced stress.** HeLa
1172 cells were transfected with GFP-2xFYVE^{Hrs} for 24 hr, labeled with 100 nM Mito-Red, photoirradiated
1173 as before, and then imaged live. Images were acquired immediately post-laser (0 min) and after 60 min.
1174

1175 **Figure 10. Localization of Rabex-5 and Alsin upon mitochondrial stress.**

1176 BAC GFP-Rab5 cells seeded on gridded dishes were labeled with 100 nM Mito-Red and
1177 photoirradiated as before. Cells were fixed after 30 min post-laser treatment and immunostained with
1178 antibody against Rabex-5 (**A**) or Alsin (**B**). Inset regions are shown. Scale bars, 10 μ m. (**C**)
1179 Colocalization analysis from untreated and laser-treated cells in (**A**) and (**B**), $n = 3$. P-values based on
1180 two-tailed t-tests.

1181

1182 **Figure 10-figure supplement 1. Endogenous localization of Rabex-5 and Alsin.** BAC GFP-Rab5
1183 cells were seeded on glass coverslips, fixed, and immunostained with specific antibodies against
1184 Rabex-5 (**A**) or Alsin (**C**). Inset regions are shown. Scale bars, 10 μ m. (**B**) A schematic representation
1185 of the domain organization of human Alsin. The regulator of chromosome condensation 1 (RCC1), B-
1186 cell lymphoma (Dbl) homology (DH) and pleckstrin homology (PH), membrane occupation and
1187 recognition nexus (MORN) motif, and vacuolar protein sorting 9 (VPS9) domains are labeled. Three
1188 putative GEF domains are annotated.

1189

1190 **Figure 10-figure supplement 2. Over-expression of Alsin or Rab5 blocks caspase-3/7 activation.**

1191 (A) HeLa cells transiently expressing empty vector, Alsin, or Rab5 were incubated in the presence of
1192 500 μM H_2O_2 and 5 μM CellEvent caspase-3/7 green detection reagent at 37°C for 2 hr. Nucleus was
1193 stained with DAPI (blue). Images were acquired by confocal microscopy. Caspase-activated cells
1194 displayed green signals, while non-activated cells (PBS control) showed no signal. Percent of cells
1195 with positive signals were quantified in (B), $n = 50$. Error bars represent SEMs. Scale bars, 10 μm .

1196

1197 **Figure 11. Alsin is required for Rab5 recruitment and regulates cytochrome c release.** (A) Flow

1198 chart depicting the different stages and time (in days) from induced-pluripotent stem cells (iPSC), to
1199 neuroprogenitor cells (NPC), and to mature spinal motor neurons (sMN). The small molecules and
1200 compounds used at different stages are shown and color-coded. (B) WT and Alsin^{-/-} cells were

1201 challenged with either PBS (Ctrl) or 100 μM H_2O_2 at 37°C for 1 hr. Cells were fixed and
1202 immunostained with Rab5 and TOM20 antibodies. Inset images show are shown. Scale bars, 10 μm .

1203 (C) Subcellular fractionation of mitochondrial (Mito) and cytosolic (C) fractions from WT and Alsin^{-/-}
1204 iPSC-sMN challenged with either PBS or 100 μM H_2O_2 at 37°C for 1 hr. Protein samples were loaded

1205 onto SDS-PAGE and immunoblotted with antibodies against Rab5, tubulin and TOM20. (D) Cytosolic
1206 fractions were prepared from WT and Alsin^{-/-} iPSC-sMN challenged with 100 μM H_2O_2 at 37°C for 1

1207 hr. Densitometric quantification of cytosolic cytochrome c were collected from three independent

1208 experiments. Y-axis corresponds to normalized ratio intensity of cytochrome c to tubulin. Error bars

1209 represent SEMs. P-values based on two-tailed t-tests.

1210

1211 **Figure 11–figure supplement 1. Validation of the CRISPR/Cas9 *Alsin*^{-/-} cells in iPSC, NPC and**
1212 **iPSC-sMN. (A)** Electrophoresis result of the PCR reaction using primers flanking exon 3 and within
1213 exon 3. Homozygous deletion was confirmed by the absence of a 2.8 kb. **(B)** Protein lysates from WT
1214 KOLF and *Alsin*^{-/-} iPSC were loaded onto SDS-PAGE and immunoblotted with *Alsin* antibody. A
1215 band detected at ~184 kDa, but absent in *Alsin*^{-/-}, corresponds to full-length *Alsin*. **(C)** WT KOLF,
1216 *Alsin*^{-/-} iPSC, and neuroprogenitor cells (NPC) were immunostained with pluripotency markers Oct4
1217 and Lin28, and neuroprogenitor markers Sox2 and Pax6, respectively. **(D-E)** WT KOLF and *Alsin*^{-/-}
1218 iPSC-sMN were immunostained with motor neuron markers such as ChAT, HB9, and ISL1, nuclear
1219 dye DAPI, and cytoskeletal marker MAP2. **(F)** WT KOLF and *Alsin*^{-/-} iPSC-sMN were immunostained
1220 with antibodies against Rab5 and *Alsin*, along with DAPI (nuclear) and phalloidin (actin) stains. Scale
1221 bars, 10 μm.

1222
1223 **Figure 12. Schematic model depicting the role of Rab5-*Alsin*-mitochondria during oxidative**
1224 **stress.** In the normal condition, mitochondria (Mito, red) are elongated and tubular (left). Rab5 (green)
1225 are localized on early endosomes (EE) to assemble the Rab5 machinery for endosomal maturation and
1226 membrane trafficking. At steady state, some EE make transient contacts with mitochondria. During
1227 oxidative stress (e.g.. laser- or chemically-induced), mitochondria undergo MOMP and a dramatic
1228 morphological transformation into rounded and swollen structures (right). The release of the apoptotic
1229 factor, cytochrome c, from mitochondria into the cytosol is associated with a re-localization event of
1230 Rab5 from EE to mitochondria via a cytosolic intermediate, accompanied by an increase in EE-
1231 mitochondria MCS. The recruitment and activation of Rab5 on mitochondria depend on the Rab5 GEF
1232 *Alsin* (blue), which leads to a selective recruitment of Rabenosyn-5 (light green). This signaling

1233 cascade on mitochondria is a reversible process that regulates the apoptotic program (e.g. cytochrome c
1234 release and caspase activation) and thus, promotes overall cell survival.

1235

1236 **Video 1. Dynamics of transferrin and mitochondria.** HeLa cells were labeled with Alexa-488
1237 transferrin (Tf; green) and Mito-Red (Mito; red). Images were acquired using a spinning disk confocal
1238 microscope at 11 frames/sec for ~6 min. Time stamp corresponds to min:sec:msec.

1239

1240 **Video 2. Dynamics of transferrin and mitochondria.** Zoom-in of a HeLa cell labeled with Alexa-
1241 488 transferrin (Tf; green) and Mito-Red (Mito; red). The movement of endosomes during a
1242 mitochondria fission event is shown. Images were acquired using a spinning disk confocal microscope
1243 at 11 frames/sec for ~5 min. Time stamp corresponds to min:sec:msec.

1244

1245 **Video 3. Dynamics of Rab5-positive endosomes and mitochondria.** Zoom-in of a BAC GFP-Rab5
1246 (green) cell labeled with Mito-Red (Mito; red). Images were acquired using a spinning disk confocal
1247 microscope at 11 frames/sec for ~4 min. Time stamp corresponds to min:sec:msec.

1248

1249 **Video 4. Mitochondria dynamics during laser-induced stress.** HeLa cells were labeled with Mito-
1250 Red and photoirradiated via 561 nm laser for 1 min, and immediately imaged. Time-lapse was
1251 acquired using a spinning disk confocal microscope at 11 frames/sec for ~5 min.

1252

1253 **Video 5. GFP-Rab5 recruitment to mitochondria during laser-induced stress.** Zoom-in of a BAC
1254 GFP-Rab5 (green) cell labeled with Mito-Red (Mito; red). Images were acquired using a spinning disk
1255 confocal microscope at 11 frames/sec with 1 min increment for ~30 min.

1256

1257 **Video 6. Endosomes and mitochondria interactions upon laser-induced stress.** BAC GFP-Rab5
1258 (green) cells were labeled with Mito-Red (red) and photoirradiated via 561 nm laser for 1 min, and
1259 then imaged after 5 min. Time-lapse was acquired using a spinning disk confocal microscope for 20
1260 frames with 5 sec increment for ~3 min. Boxed regions indicate GFP-Rab5 endosomes docking onto
1261 mitochondria.

1262

1263 **Video 7. Endosomes and mitochondria interactions upon laser-induced stress.** Zoom-in of a BAC
1264 GFP-Rab5 (green) cell labeled with Mito-Red (Mito; red) and photoirradiated via 561 nm laser for 1
1265 min, and then imaged continuously for ~5 min. Images were acquired using a spinning disk confocal
1266 microscope at 11 frames/sec.

1267

1268 **Video 8. Mitochondria dynamics during H₂O₂-induced stress.** HeLa cells were labeled with Mito-
1269 Red and then imaged in the presence of 250 μM H₂O₂ for ~60 min. Time-lapse was acquired using a
1270 spinning disk confocal microscope for 50 frames with 2 min increment.

1271

1272 **Figure 1D,E–source data.** Numerical data corresponding to the graphs presented in Figure 1D,E.

1273

1274 **Figure 2B–source data.** Numerical data corresponding to the bar graphs presented in Figure B.

1275

1276 **Figure 2D–source data.** Numerical data corresponding to the line trace presented in Figure 2D.

1277

1278 **Figure 4I–source data.** Numerical data corresponding to the bar graphs presented in Figure 4I.

1279

1280 **Figure 4–figure supplement 3B,C-source data.** Numerical data corresponding to the bar graphs
1281 presented in Figure 4–figure supplement 3B,C.

1282

1283 **Figure 5C,D–source data.** Numerical data corresponding to the bar graphs presented in Figure 5C,D.

1284

1285 **Figure 5G–source data.** Numerical data corresponding to the line traces presented in Figure 5G.

1286

1287 **Figure 6B–source data.** Numerical data corresponding to the bar graph presented in Figure 6B.

1288

1289 **Figure 6C–source data.** Numerical data corresponding to the chart presented in Figure 6C.

1290

1291 **Figure 6E–source data.** Numerical data corresponding to the bar graphs presented in Figure 6E.

1292

1293 **Figure 7C–source data.** Numerical data corresponding to the line traces presented in Figure 7C.

1294

1295 **Figure 8C–source data.** Numerical data corresponding to the bar graphs presented in Figure 8C.

1296

1297 **Figure 9C–source data.** Numerical data corresponding to the bar graphs presented in Figure 9C.

1298

1299 **Figure 10C–source data.** Numerical data corresponding to the bar graphs presented in Figure 10C.

1300

1301 **Figure 10–figure supplement 2B-source data.** Numerical data corresponding to the bar graphs
1302 presented in Figure 10–figure supplement 2B.

1303

1304 **Figure 11D–source data.** Numerical data corresponding to the line traces presented in Figure 11D.

1305

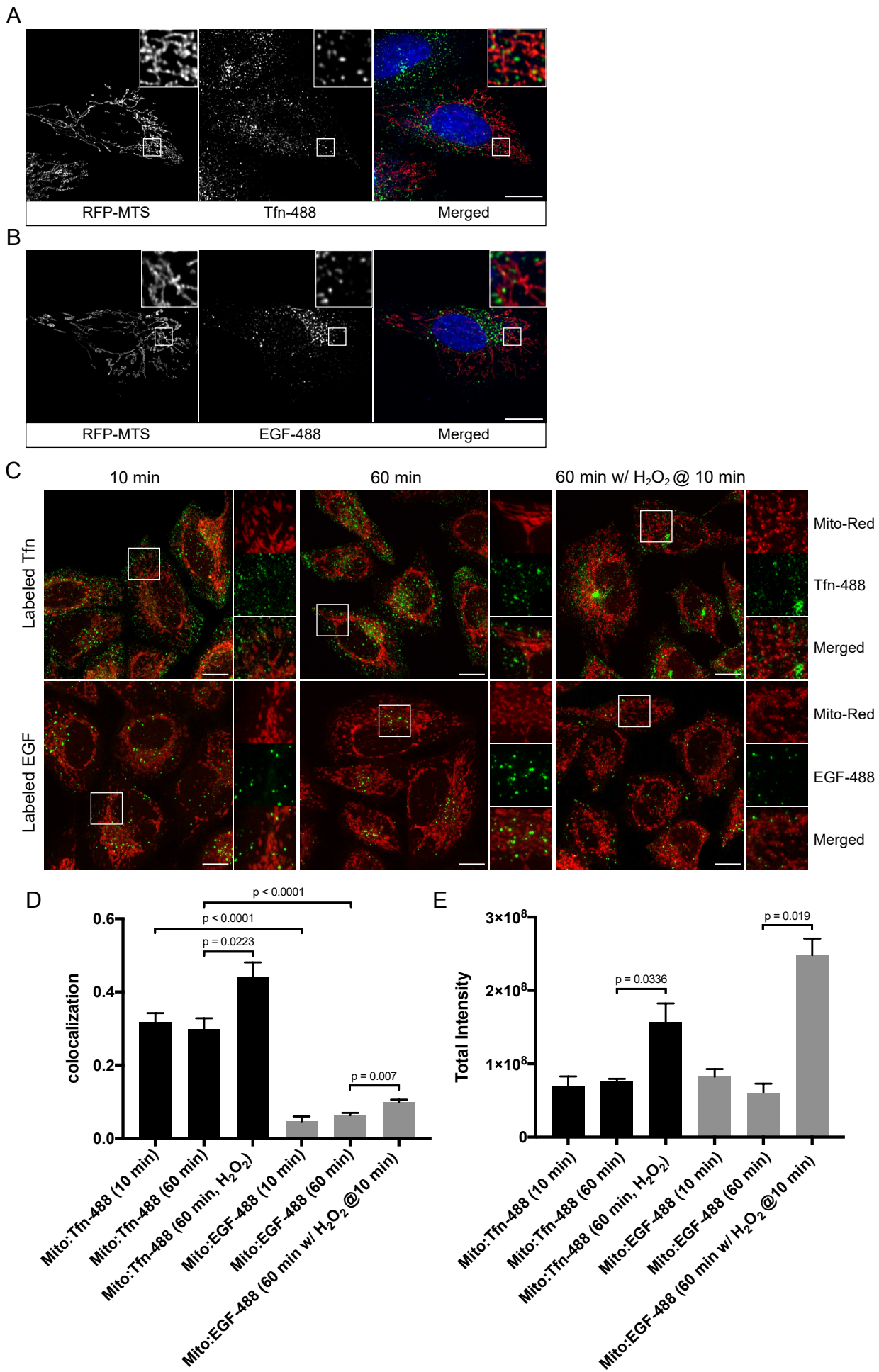


Figure 1

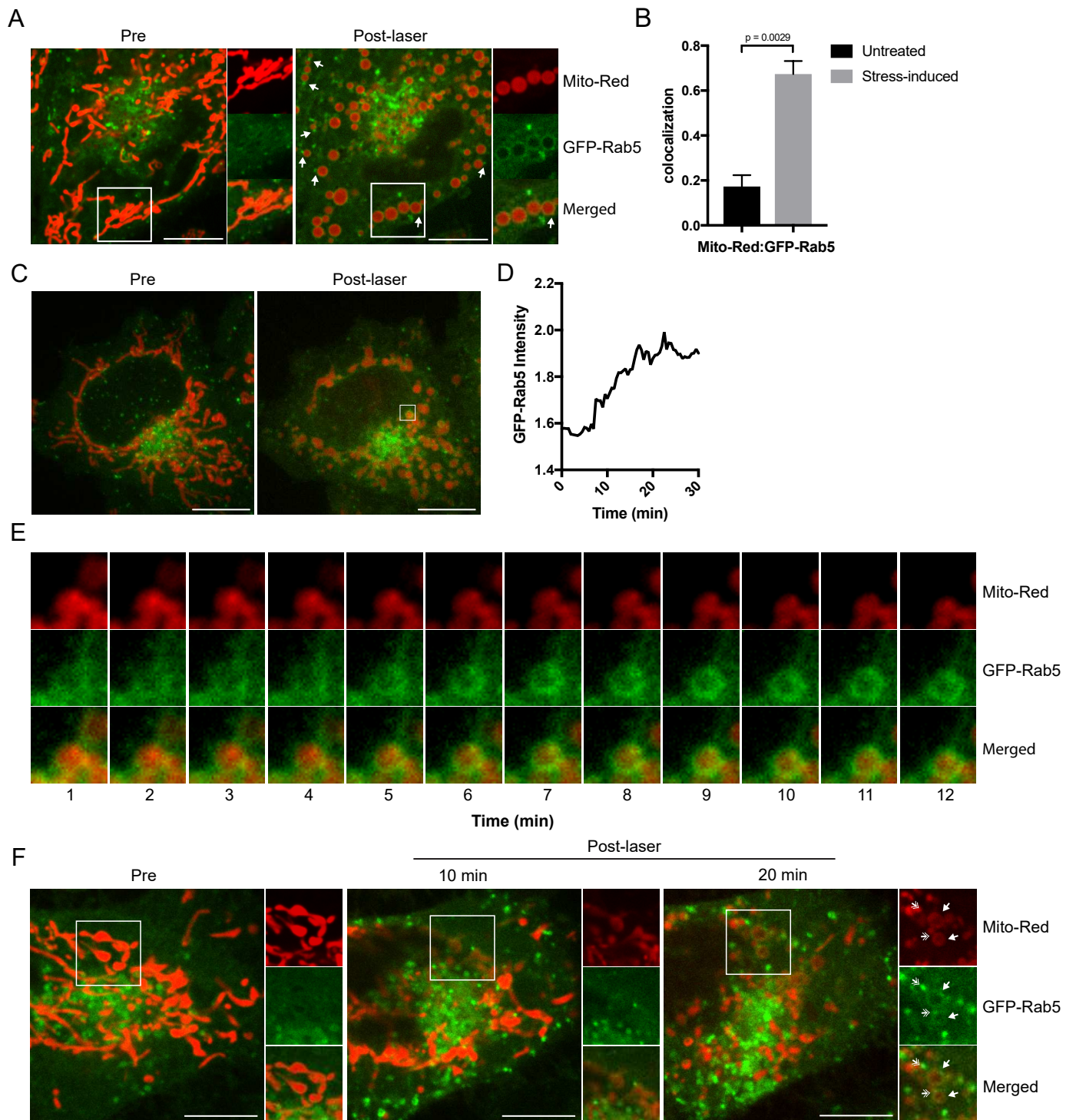


Figure 2

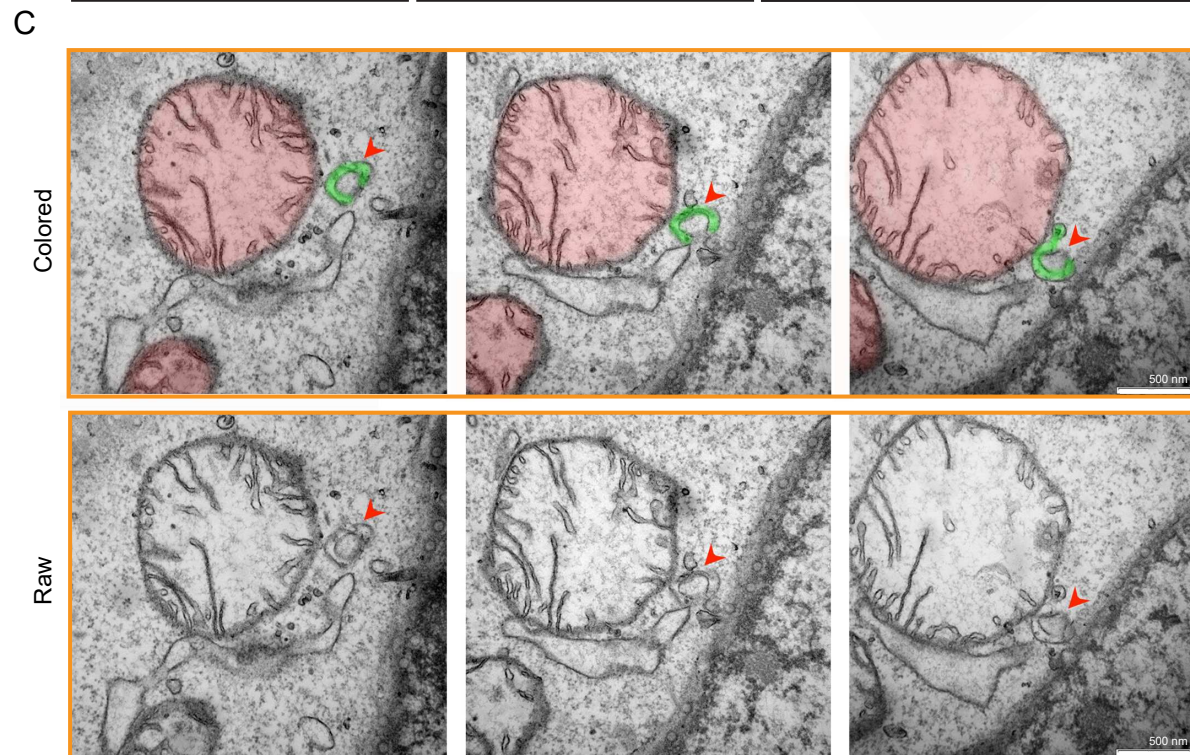
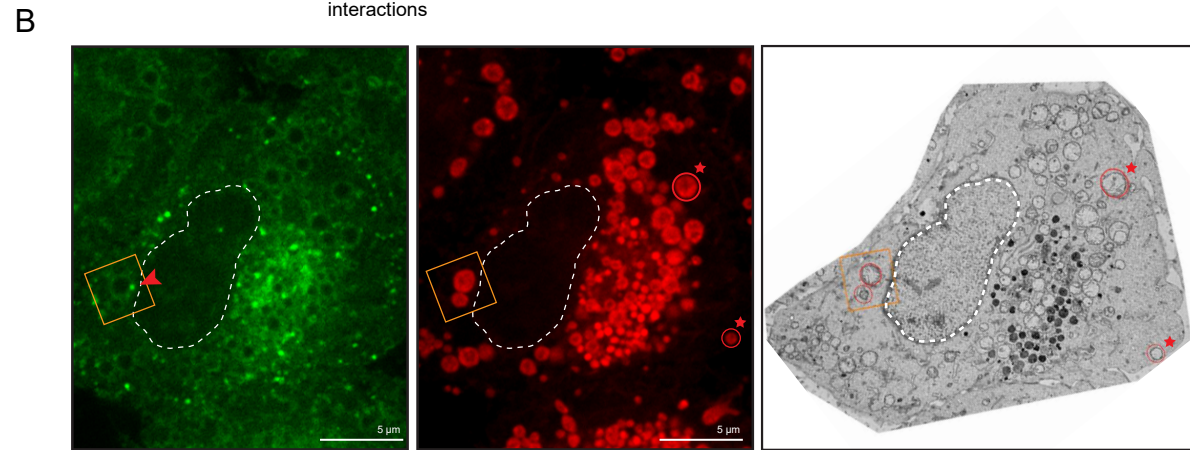
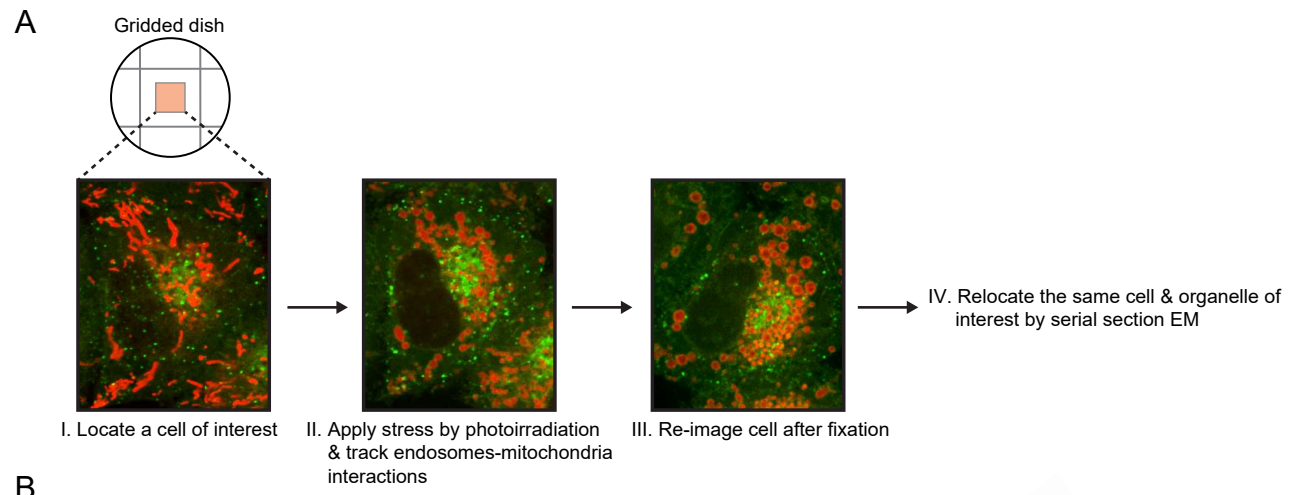


Figure 3

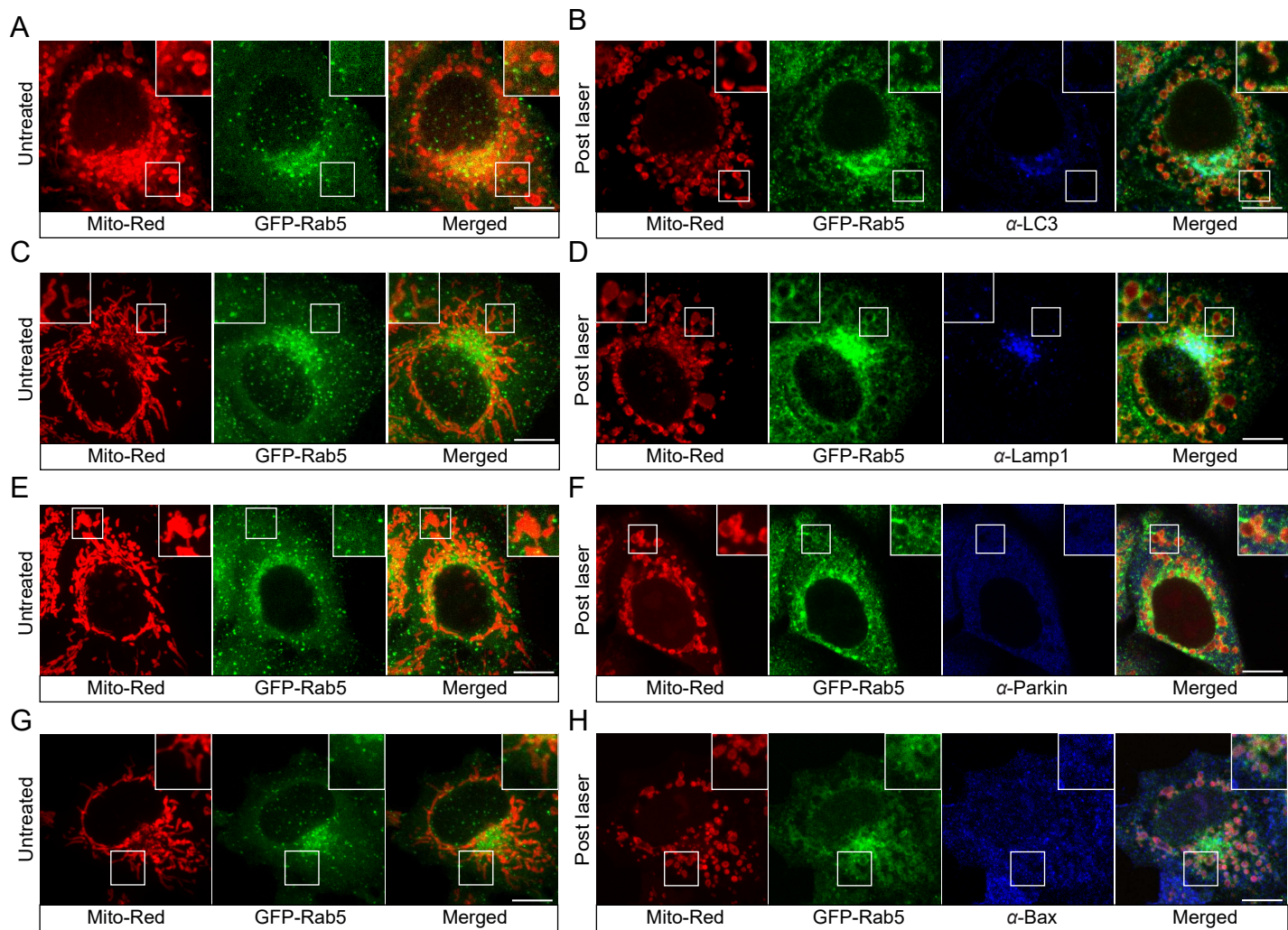
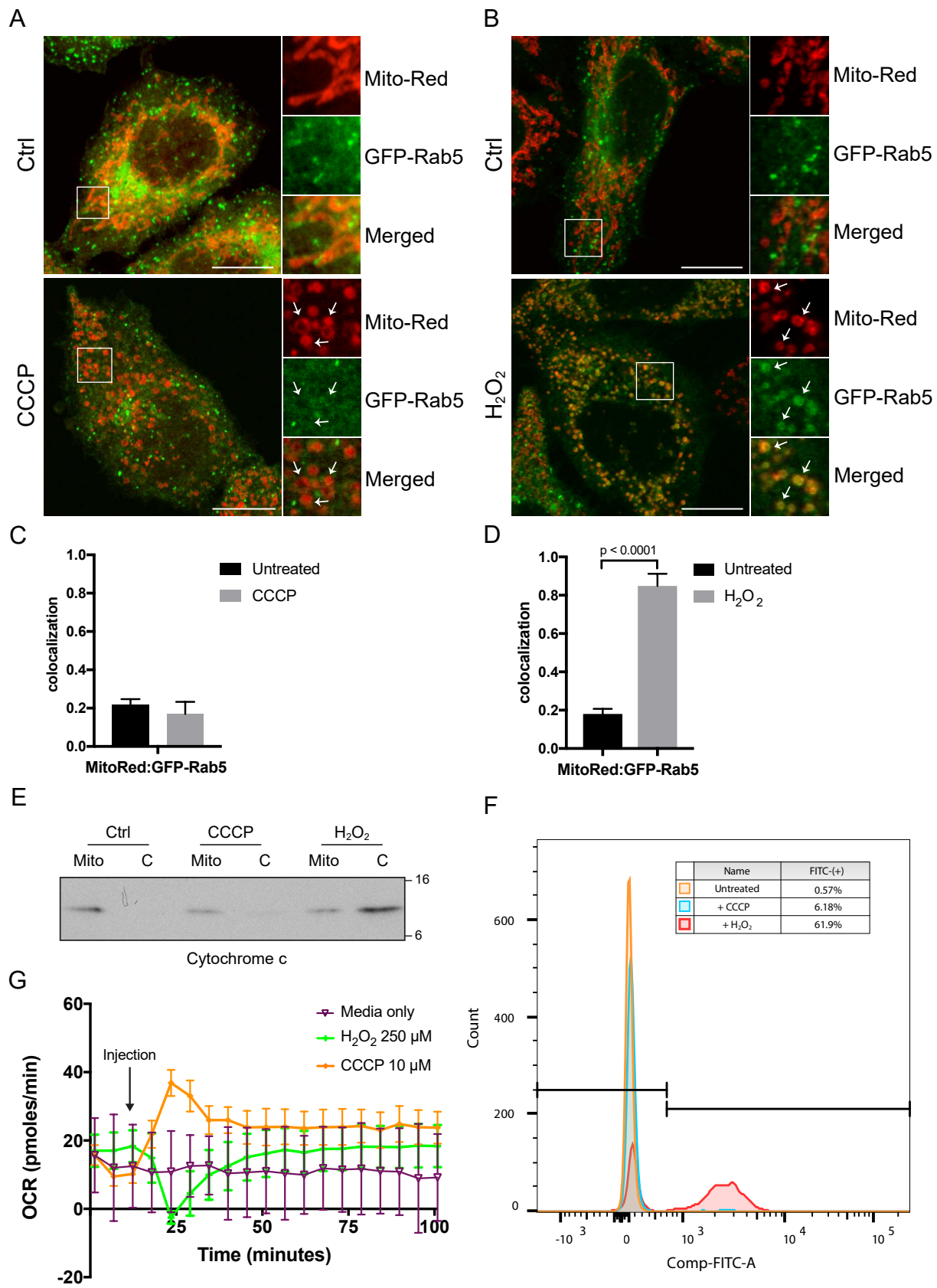


Figure 4



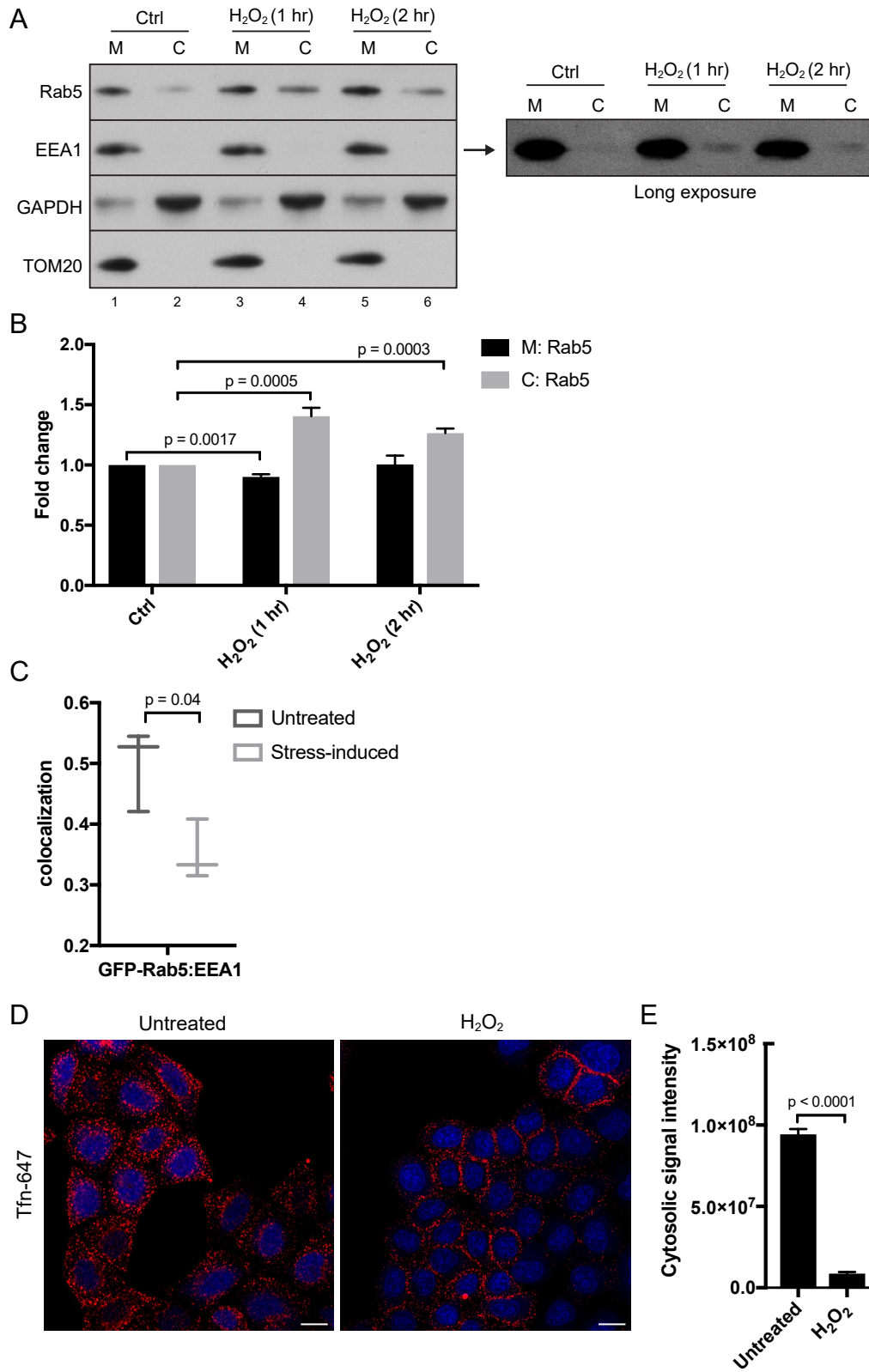


Figure 6

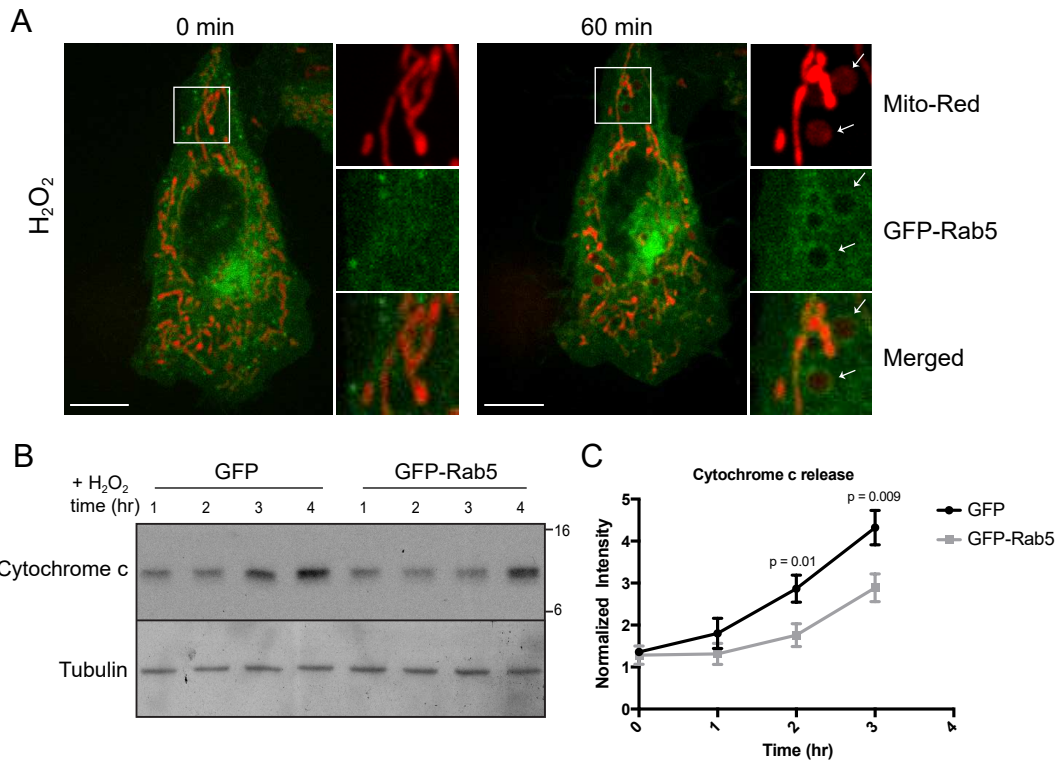


Figure 7

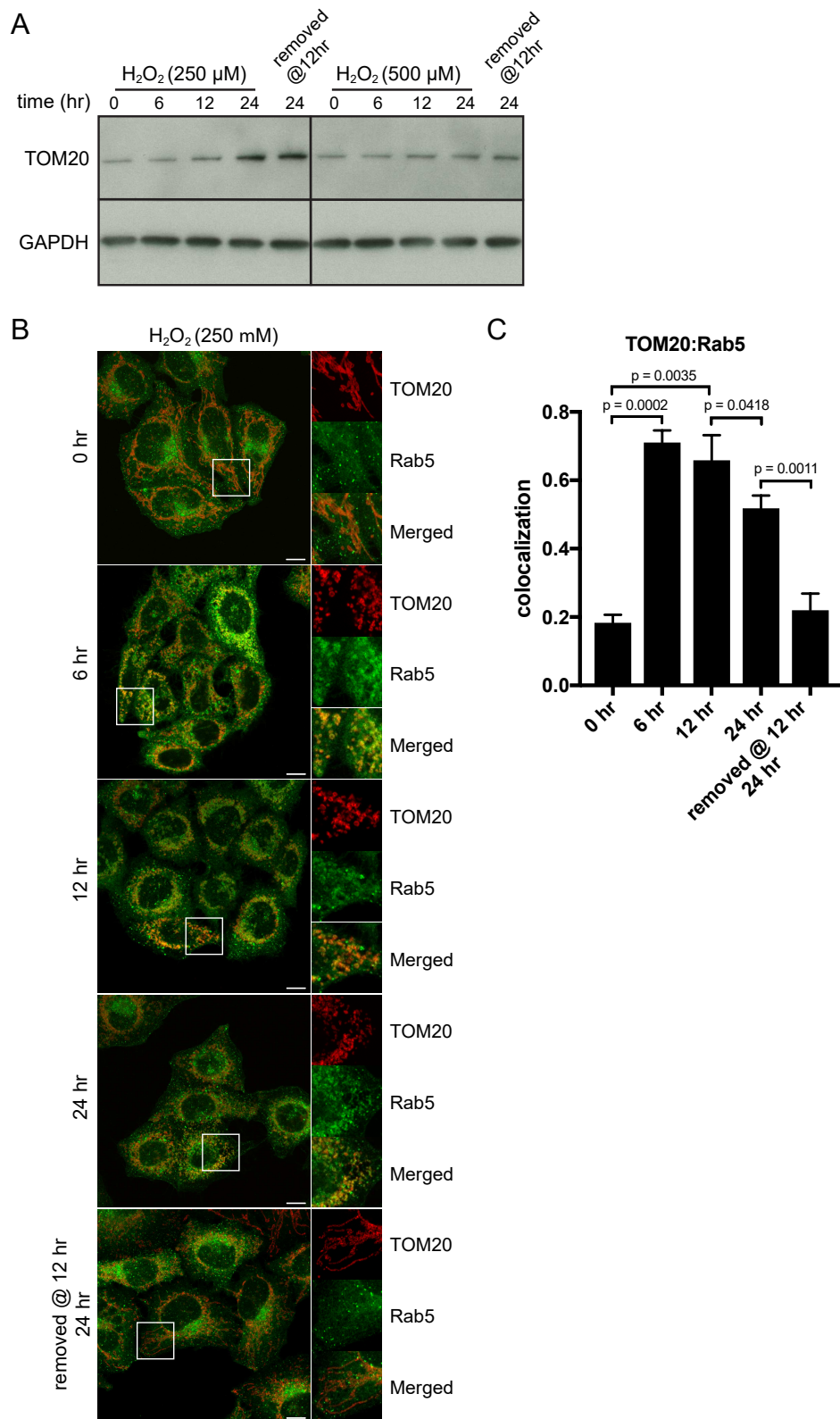


Figure 8

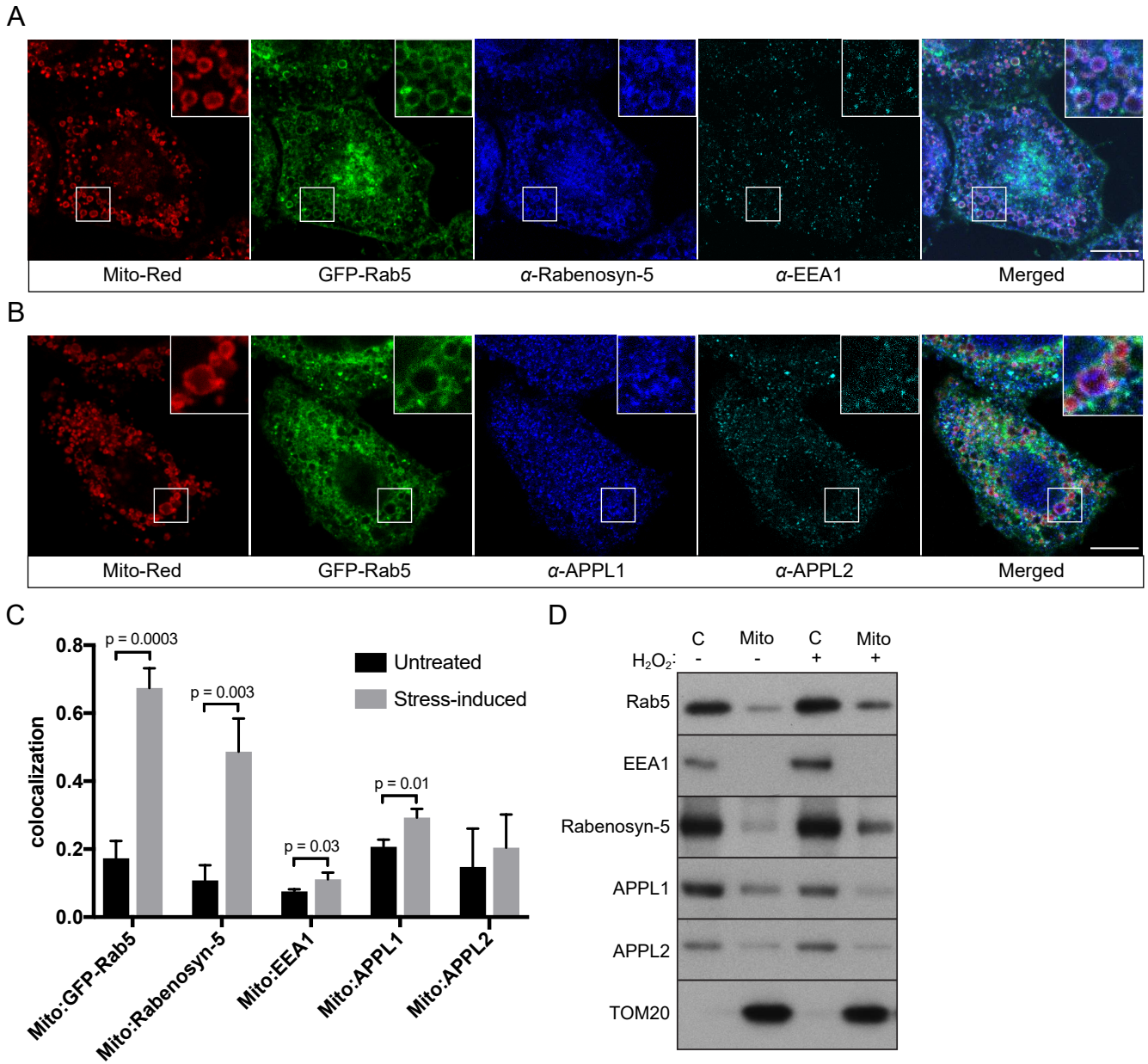


Figure 9

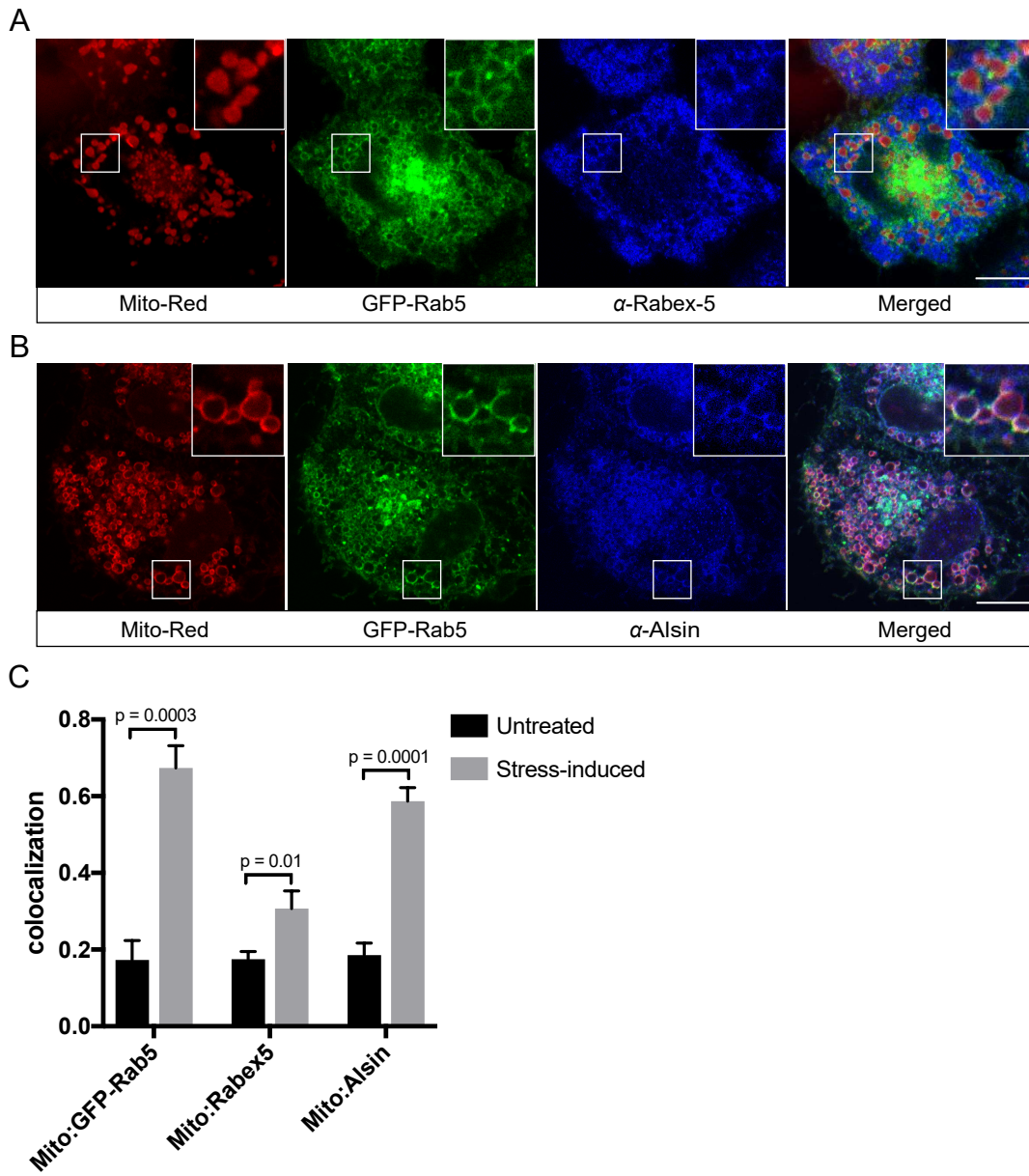


Figure 10

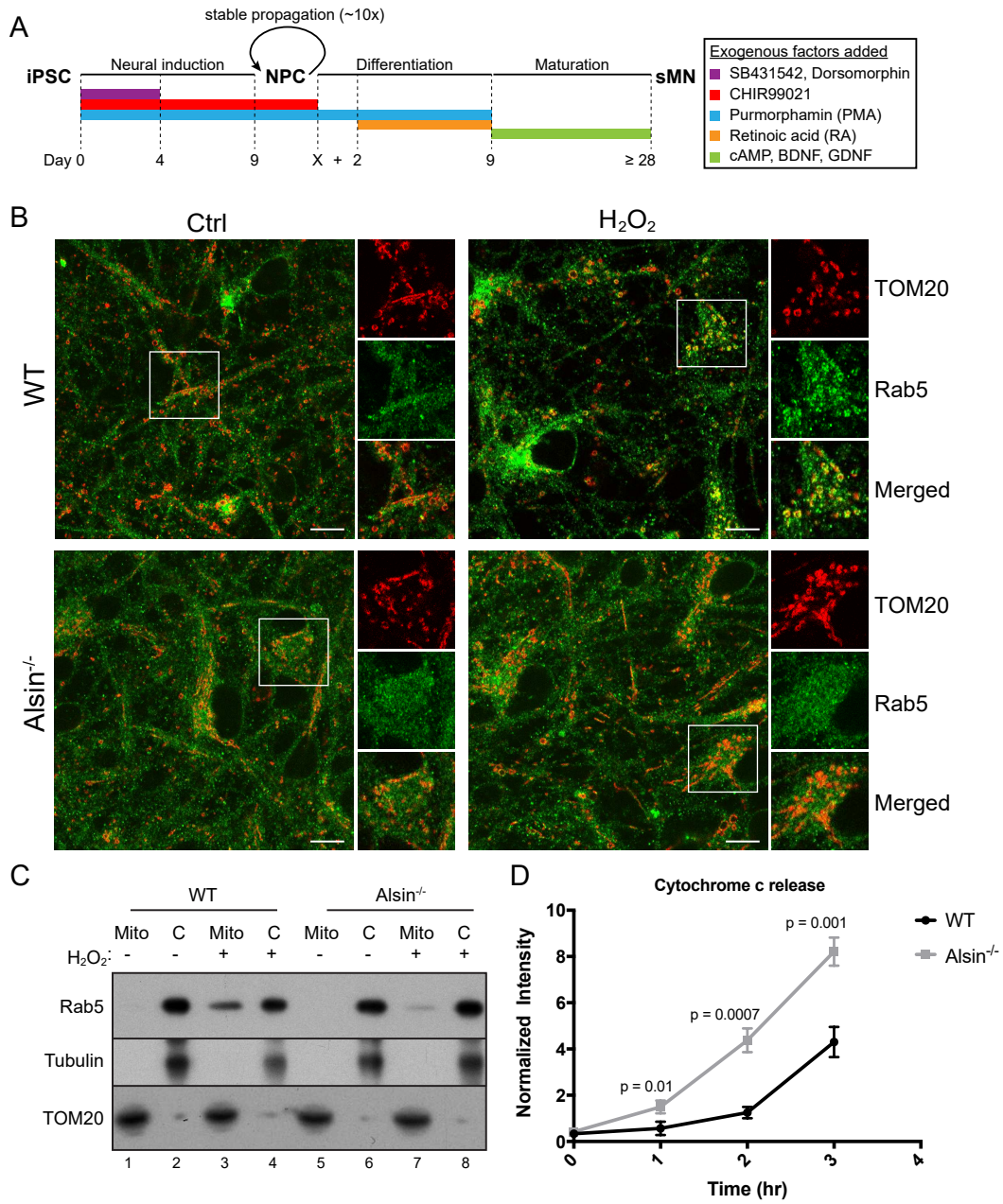


Figure 11

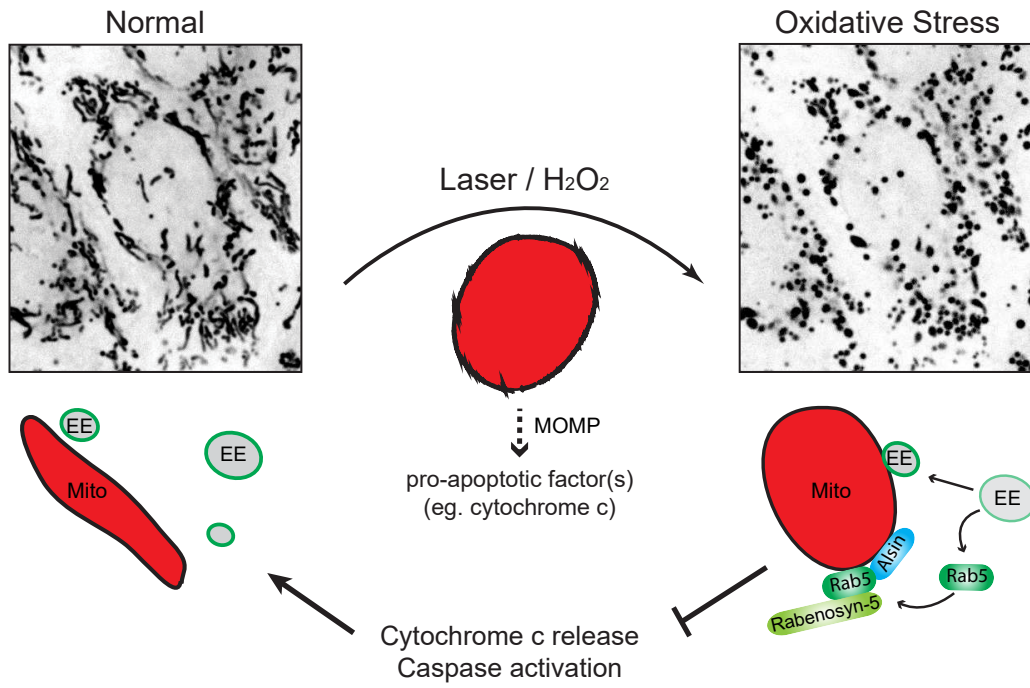


Figure 12